WILEY-VCH

DOI: 10.1002/ ((please add manuscript number))
Article type: Full paper

Influence of dopant size and electron affinity on the electrical conductivity and thermoelectric properties of a series of conjugated polymers

*Zhiming Liang, Yadong Zhang, Maryam Souri, Xuyi Luo, Alex M. Boehm, Ruipeng Li, Yan Zhang, Tairan Wang, Doo-Young Kim, Jianguo Mei, Seth R. Marder, Kenneth R. Graham**

Z. Liang, A. M. Boehm, Yan Zhang, Prof. D.-Y. Kim, Prof. K. R. Graham
Department of Chemistry, University of Kentucky, Lexington, Kentucky 40506, USA
E-mail: kenneth.graham@uky.edu
Dr. Y. Zhang, Prof. S. R. Marder
School of Chemistry and Biochemistry and Center for Organic Photonics and Electronics, Georgia Institute of Technology, Atlanta, Georgia 30332, USA
M. Souri
Department of Physics, University of Kentucky, Lexington, Kentucky 40506, USA
X. Luo, Prof. J. Mei
Department of Chemistry, Purdue University, West Lafayette, Indiana 47907, United States
Dr. R. Li
Brookhaven National Laboratory, Shirley, New York 11967, USA
T. Wang
School of Physics and Telecommunication, South China Normal University, Guangzhou 510000, P.R. China

Keywords: conducting polymer, organic thermoelectric, doping, photoelectron spectroscopy, charge transport

Chemical doping is widely used to manipulate the electrical and thermoelectric properties of organic semiconductors, yet intelligent design of polymer-dopant systems remains elusive. It is challenging to predict the electrical and thermoelectric properties of doped organic semiconductors due to the large number of variables impacting these properties, including film morphology, dopant and polymer energetics, dopant size, and degree of polaron delocalization. Herein, a series of dopants with varying sizes and electron affinities (EAs) are combined with polymers of differing ionization energies (IEs) to investigate how the difference between polymer IE and dopant EA influences the doping efficiency and electrical conductivity, and how the dopant size influences the thermoelectric properties. Our experiments demonstrate that at low doping levels the doping efficiency strongly depends on

the difference between the polymer IE and dopant EA; the effectiveness of doping on increasing electrical conductivity drastically decreases at high loadings for the molybdenum dithiolene complexes, while $FeCl_3$ remains effective at high loadings; and the large molybdenum complexes lead to more delocalized polarons as compared to $FeCl_3$. To take advantage of the complementary doping characteristics of the molybdenum complexes and $FeCl_3$, both dopants are employed simultaneously to reach high power factors at relatively low dopant concentrations.

1. Introduction

Organic semiconductors are appealing for use in light-emitting diodes (OLEDs),[1, 2] transistors,[3-5] photovoltaics,[6, 7] and thermoelectrics (TEs)[8, 9] due to their readily modified electrical and optical properties,[10] mechanical flexibility,[11] and solution processability.[12] Chemical doping (i.e., introducing free charge-carriers through the addition of a molecule that oxidizes or reduces the organic semiconductor) is particularly important in OLEDs, where doped transport layers are used in to improve charge injection,[13, 14] and in TEs, where dopants are used to manipulate both the electrical conductivity (σ) and Seebeck coefficient (α).[15, 16] Controllably altering the electrical properties in chemically doped organic semiconductors is a major challenge. As opposed to doping in inorganic semiconductors, where the crystalline structure is largely unaffected by the incorporation of dopant atoms and the high dielectric constants and electronic band structures lead to highly delocalized charges, dopant incorporation into organic semiconductors significantly disrupts the morphology, alters the microstructure, and leads to charge-carriers with varying degrees of localization.[17-20] Furthermore, the doping efficiency (i.e., the fraction of dopants that lead to charge-carriers) in organic semiconductors can be significantly less than unity and difficult to quantify. Selecting and designing dopants to achieve specific properties in films of organic semiconductors is thus a challenging area where more basic understanding is necessary.

Since the field of π-conjugated polymers (πCPs) began with the discovery that πCPs could be made to have high electrical conductivities through chemical or electrochemical doping,[21-23] a consistent search for high performing dopants and polymers has continued. A number of different p-type dopants have received widespread attention due to their ability to effectively dope solution processed πCPs and lead to high electrical conductivities, including $FeCl_3$,[24, 25] I_2,[26, 27] $Mo(tfd)_3$,[28] and F4TCNQ and its derivatives[18, 19, 29-31]. Many factors that influence the electrical properties of doped πCPs are roughly understood. For example, the electrical properties are highly dependent on the doping efficiency, film morphology,[17, 18, 30, 32, 33] doping mechanism (ground state charge-transfer complex vs. integer charge transfer)[32, 34] and the polaron-anion coulombic attraction; however, the details and interrelationships between these parameters must be further understood to help guide the development of higher performing materials.

The doping efficiency of a given polymer-dopant system will be determined by two primary variables. The first variable expected to influence the doping efficiency is the difference between the polymer ionization energy (IE) and dopant electron affinity (EA) for p-doped polymers, or the polymer EA and dopant IE for n-doped polymers.[35] For p-dopable polymers, the doping efficiency should generally increase as the $IE_{polymer}$ - EA_{dopant} difference increases and results in a larger thermodynamic driving force for polymer oxidation.[36, 37] For example, Karpov *et al.* showed that when a high IE polymer (IE = 5.49 eV) is doped with a high EA dopant, hexacyano-trimethylene-cyclopropane (EA = 5.87 eV), the electrical conductivity is more than two orders of magnitude higher than when a lower EA dopant is used, F4TCNQ (EA = 5.24eV).[32, 35] Another factor determining the doping efficiency is the dopant miscibility with the polymer.[17, 38-41] As the dopant molecules aggregate and phase separate from the polymer, they no longer efficiently dope the polymer. As a prime example, Schlitz *et al.* showed that σ for an n-doped polymer, poly{N,N′-bis(2octyl-dodecyl)-1,4,5,8-

napthalenedicarboximide-2,6-diyl]-alt-5,5′-(2,2′-bithiophene), is limited by the miscibility of the n-type dopants, dihydro-1H-benzoimidazol-2-yl derivatives, with the polymer.[39]

Influential aspects of the morphology on the electrical conductivity include the degree of polymer crystallinity,[18, 42, 43] the size of the crystalline domains,[17, 33] the effect of the dopant on the crystalline packing,[30, 32] and the dopant distribution within the film (e.g., whether the dopant is primarily in the crystalline or amorphous regions).[17, 18, 48] The morphology of the doped film will depend largely on the processing conditions, the ability of the polymer to crystallize, and the interactions between the polymer and dopant. In doped regioregular poly(3-hexylthiophene) (RR-P3HT), the electrical conductivity can vary by over an order of magnitude depending on the degree of crystallinity.[18, 42-44] Typically, single-solution doping, whereby the polymer and dopant are both mixed together in solution, can lead to more disconnected crystallites compared with films of the pure polymer.[17] A sequential processing strategy, whereby the pure polymer film is first cast and then exposed to a solution of the dopant, has recently been explored to maintain highly connected polymer crystalline domains upon dopant addition.[17, 18, 37] F4TCNQ doped RR-P3HT films prepared through sequential doping show electrical conductivities that are approximately an order of magnitude higher than films prepared through a standard single-solution doping method at the same doping concentrations.[17, 18, 34]

The extent of polaron delocalization will highly impact the electrical conductivity, and will be determined by the polymer or oligomer packing, the degree of crystallinity, oligomer or polymer molecular weight, and the polaron-anion separation distance. Comparing previous experimentally measured charge-modulated absorbance spectra with the theoretically calculated spectra, Ghosh, *et al.* showed that the degree of polaron delocalization in P3HT varies with both molecular weight and the degree of disorder.[45] Through using optical absorbance measurements in the near-IR region on chemically doped P3HT films of varying degrees of crystallinity, it was demonstrated that higher degrees of polaron delocalization

translate into higher electrical conductivities.[18] The effects of polaron delocalization are also apparent across different polymer families. For example, by comparing the photoinduced absorption spectra of polarons and the mobility of RRa-P3HT, RR-P3HT, methylated ladder-type poly(para-phenylene), poly(9,9-dioctyl)fluorine, and poly(phenylene-vinylene), Wohlgenannt *et al.* conclude that more delocalized polarons result in higher charge-carrier mobility and higher electrical conductivity.[46]

The doping mechanism can also vary based on the organic semiconductor and dopant used.[32, 36, 47] Here, the doping mechanism refers primarily to whether a charge-transfer complex is formed or whether integer charge transfer occurs. In the case that integer charge transfer occurs, the polaron-anion binding energy of the ion pair should influence the electrical conductivity, as smaller polaron-anion coulombic interaction energies should lead to more delocalized polarons and higher charge-carrier mobilities.[46, 48, 49] Although most work has focused on how polymer structure and degree of crystallinity affect polaron delocalization, we expect that dopant size is one of the key variables that will influence the separation between the center of charge on the polymer and dopant, and thus the coulombic interaction energy.

The above discussion highlights some of the complexities of how dopants influence the electrical conductivity in conjugated polymers, but this is only a portion of the required knowledge needed to design more efficient thermoelectric polymer-dopant systems. In thermoelectrics, the power factor will depend on the product of the electrical conductivity (σ) and the Seebeck coefficient squared (α^2). Thus, it must also be understood how the dopant influences the Seebeck coefficient. To create high-performing thermoelectric materials the effects of doping on both the electrical conductivity and Seebeck coefficient must be balanced to create the highest power factor ($P=\sigma\alpha^2$). For example, through controlling the degree of oxidation in poly(3,4-ethylenedioxythiophene) with tosylate and

tetrakis(dimethylamino)ethylene, Bubnova *et al.* were able to reach power factors of 320 μW m^{-1} K^{-2} at intermediate values of both σ and α.[15]

In this work we investigate the effects of dopant size and EA on the electrical conductivity and Seebeck coefficient of p-doped conjugated polymers with varying IEs. The dopants include $Mo(tfdCO_2Me)_3$, $Mo(tfd)_3$, and $FeCl_3$. $Mo(tfdCO_2Me)_3$ and $Mo(tfd)_3$ are both relatively large dopants in size (~11-14 Å diameters) with high EAs of 5.30 eV and 5.51 eV (as measured with IPES), while $FeCl_3$ is smaller in size (~3 Å diameter) and has a much lower EA of 4.65 eV (as determined electrochemically). As the doping efficiency is expected to vary with the difference between the polymer IE and dopant EA, we investigate polymers with IEs spanning from 4.56 to 5.08 eV, including RR-P3HT, RRa-P3HT, PDPP-4T and PDPP-T-TT-T as shown in **Figure 1**. Furthermore, we apply UV-vis-IR absorbance, Raman scattering, grazing incidence wide angle X-ray scattering (GIWAXS), and ultraviolet photoelectron spectroscopies to understand why the Mo complexes lead to significantly higher electrical conductivities and power factors at low doping concentrations. Finally, we show that different dopants can be combined to produce higher power factors than with either of the individual dopants alone.

2. Results and Discussion

2.1. Dopant and Polymer Energetics

The dopants shown in Figure 1a are selected for their varying sizes and EAs, while the polymers shown are selected for their varying IEs and morphologies (e.g. crystalline vs. amorphous). The similar structure and charge-carrier mobilities of the diketopyrrolopyrrole (DPP) containing polymers[50-52] further allows us to isolate the influence of the difference between the polymer IE and dopant EA on the electrical conductivity. Polymer IEs were measured using low-energy (10.2 eV) ultraviolet photoelectron spectroscopy (UPS), while

dopant EAs were measured using low-energy inverse photoelectron spectroscopy (IPES) and cyclic voltammetry (CV). The use of lower energies than commonly employed in laboratory-based photoelectron spectrometers allows us to minimize sample damage and more accurately probe the material energetics.[53, 54] The measured IEs and EAs for the polymers and dopants are summarized in Figure 1b, with the UPS, IPES, and CV data for the materials shown in Figure 1c, SI **Figure S2**, Figure 1d, and SI **Figure S1**, respectively.

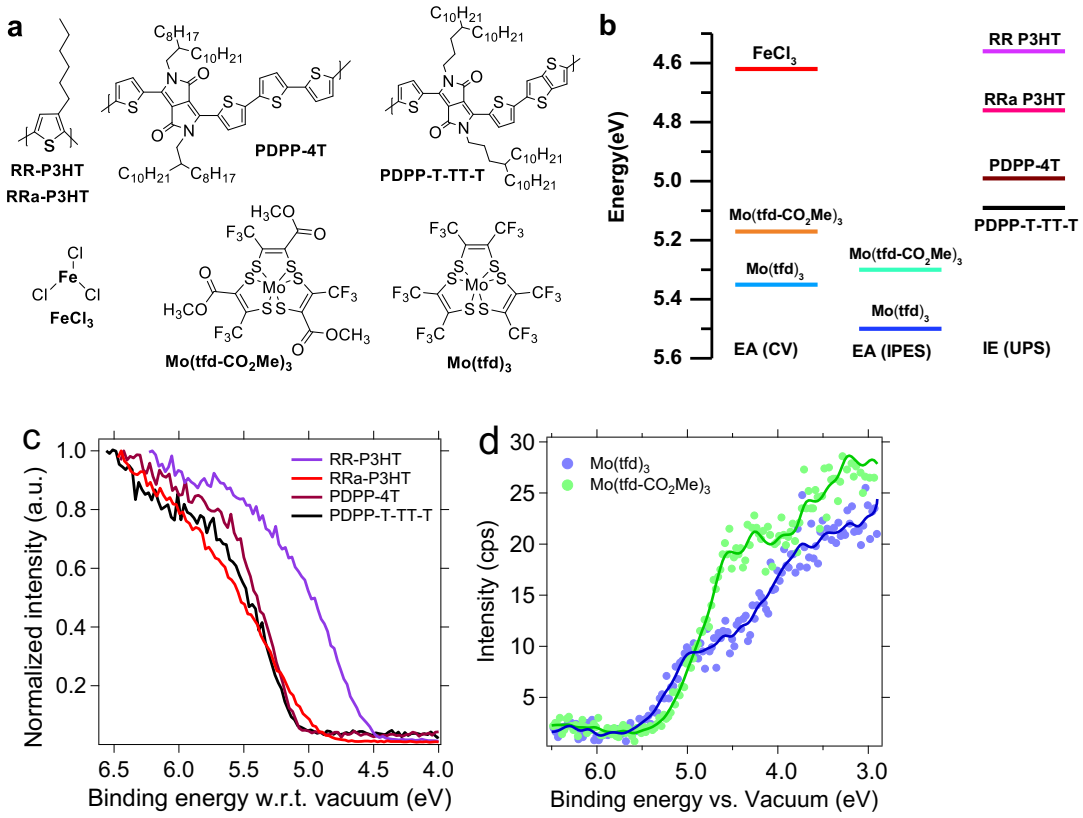

Figure 1. Molecular structures of the polymers and dopants used in this work (a), summary of polymer IEs and dopant EAs (b), UPS spectra of the HOMO onset regions of the polymers with respect to vacuum (c), and IPES spectra of the LUMO onsets of the dopants with respect to vacuum (d). The filter energy for the IPES measurements is 5.77 eV.

The UPS measured IEs correspond well with previously reported literature values.[24, 55, 56] However, the EAs of 5.51 and 5.30 we measure for $Mo(tfd)_3$ and $Mo(tfd\text{-}CO_2Me)_3$ differ slightly from the literature reported values of 5.6 and 5.0 eV.[57, 58] We expect that the differences in our EA values compared to previous reports arise from the higher resolution

(~0.3 eV compared to ~0.5 eV) and the reduced sample damage during measurement expected with our IPES system.[54] Uniform films of $FeCl_3$ for IPES measurements could not be prepared through solution processing and $FeCl_3$ appeared to decompose during thermal evaporation. This decomposition led to anonymously high EAs of 5.8 eV measured with IPES, and XPS measured stoichiometries that did not match the expected 1:3 composition of $FeCl_3$. The cyclic voltammetry measurements of $FeCl_3$ on the other hand showed that the reduction potential in chloroform was -0.48 V ($E_{1/2}$) vs. Fc/Fc^+, which can be converted to -4.62 eV vs. vacuum based on Fc/Fc^+ at -5.10 eV vs. vacuum.[59] The $E_{1/2}$ values for $Mo(tfd)_3$ and $Mo(tfd\text{-}CO_2Me)_3$ vs. Fc/Fc^+ are 0.25 V and 0.07 V for the first reductions,[28, 57, 60] which yield values of -5.35 and -5.17 eV vs. vacuum. The reduction potentials from the CV measurements for $Mo(tfd)_3$ and $Mo(tfd\text{-}CO_2Me)_3$ are within 0.16 eV of the IPES measured EA values, which builds confidence in the accuracy of both the IPES and CV determined values.

2.2 Influence of dopant EA - polymer IE difference on the electrical conductivity

The electrical conductivities of $FeCl_3$, $Mo(tfd\text{-}CO_2Me)_3$, and $Mo(tfd)_3$ doped RR-P3HT films are shown in **Figure 2**. One important trend is that at ≤5% doping concentrations σ is up to 15 times higher for RR-P3HT doped with the Mo complexes than when doped with $FeCl_3$ at the same concentration. As the electrical conductivity depends on the number of charge carriers and the charge-carrier mobility, the most likely factors leading to the enhanced electrical conductivity observed for the Mo complexes at low doping concentrations are differences in the doping efficiency and differences in the charge-carrier mobility.[61] To a first approximation, the doping efficiency should be related to the difference in polymer IE and dopant EA, while the charge-carrier mobility will be primarily influenced by the film morphology and extent of polaron delocalization.[18, 35, 48] Another important trend evidenced in Figure 2 is that σ plateaus for RR-P3HT doped with the Mo complexes at between 5 and

10%, whereas σ continues to increase for up to 30% doping with $FeCl_3$. The most likely explanation here, which will be further examined, is that the polaron concentration saturates at between 5 and 10% doping for RR-P3HT doped with the Mo complexes, while $FeCl_3$ continues to lead to additional polarons at higher doping concentrations.

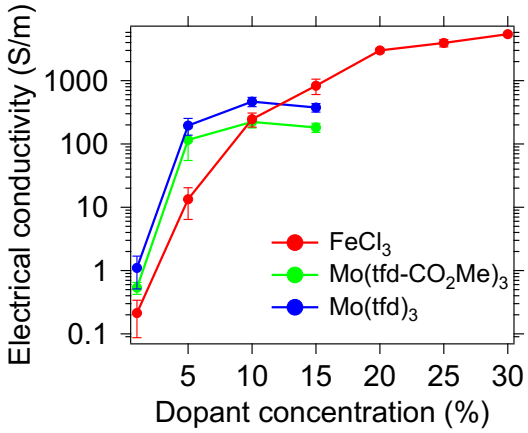

Figure 2. Electrical conductivities of $FeCl_3$, $Mo(tfd\text{-}CO_2Me)_3$, and $Mo(tfd)_3$ doped RR-P3HT as a function of the dopant concentration in mole percent relative to the polymer repeat unit. Each point is the average from 8 films produced from two fabrication runs and error bars are the standard deviations from all measurements over these 8 films.

UV-vis-Near-IR optical absorbance measurements can be used as a probe of the polaron concentrations in the various doped films, as the ratio between the neutral state absorbance band at *ca.* 510 nm and the polaron band at *ca.* 790 nm will scale directly with the concentration of polarons.[24, 25] Thus, we use these measurements as a semi-quantitative probe of doping efficiency. **Figure 3**a shows that the ratio between the polaron and neutral band continues to increase for $FeCl_3$ doped RR-P3HT up to 30% $FeCl_3$ concentration, whereas this ratio plateaus at 5 to 10% doping for the Mo complexes (Figure 3 and SI **Figure S3**). This data supports that for the Mo complexes the electrical conductivity at higher concentrations is limited by a saturation in the number of polarons. We suspect that this difference in when the polaron band saturates is due to the more limited miscibility of the Mo complexes with RR-P3HT.

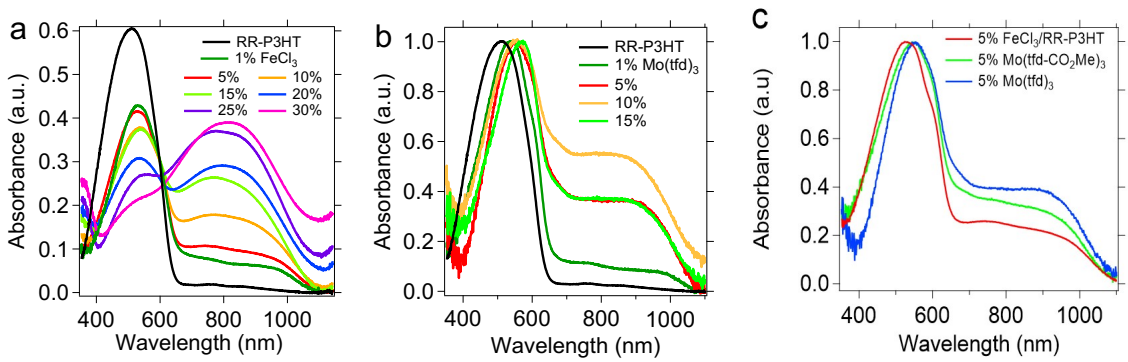

Figure 3. UV-Vis-near-IR absorbance spectra of RR-P3HT with a) $FeCl_3$ and b) $Mo(tfd)_3$ at varying dopant concentrations (by mole). c) UV-Vis-near-IR absorbance spectra of RR-P3HT doped with 5% $FeCl_3$, $Mo(tfdCO_2Me)_3$, and $Mo(tfd)_3$.

Focusing on the 5% dopant concentration (Figure 3c), where the polaron concentration is not saturated for any of the dopants, it is evident that the polaron band to neutral band absorbance ratio is largest for the $Mo(tfd)_3$ sample, followed by the $Mo(tfdCO_2Me)_3$ sample, and lowest for the $FeCl_3$ sample. This trend in the polaron band to neutral band absorbance ratio is consistent with the trend in σ, i.e., σ increases as the polaron band to neutral band absorbance ratio increases across the dopant series. The lower polaron band intensity for $FeCl_3$ is likely due to the lower EA of $FeCl_3$, which falls at nearly the same value as the IE of RR-P3HT. The lower polaron band absorbance for $Mo(tfd\text{-}CO_2Me)_3$ relative to $Mo(tfd)_3$ may be due to the higher EA of $Mo(tfd)_3$ relative to $Mo(tfd\text{-}CO_2Me)_3$, although even in the case of $Mo(tfd\text{-}CO_2Me)_3$ the large IE-EA difference of 0.7 eV is expected to be sufficient for complete dopant ionization.[31, 35, 36]

Based on the absorbance spectra there are ca. 50% more polarons in RR-P3HT doped with $Mo(tfd)_3$ as there are in RR-P3HT doped with $FeCl_3$ at 5% doping; however, σ of $Mo(tfd)_3$ doped RR-P3HT is 15 times greater than that of $FeCl_3$ at this same doping concentration. The electrical conductivity is proportional to the product of the charge-carrier mobility and the concentration of mobile charge carriers. Considering this relationship, the absorbance ratios, and the measured electrical conductivities, it appears that at low doping

concentrations the charge-carrier mobility for $Mo(tfd)_3$ doped RR-P3HT is greater than for $FeCl_3$ doped RR-P3HT. These differences in apparent charge-carrier mobilities are attributed partly to increased polaron delocalization for $Mo(tfd)_3$ doped RR-P3HT relative to $FeCl_3$ doped RR-P3HT, as will be further examined in the proceeding section.

The doping efficiencies as probed through absorbance measurements agree with expectations based purely on the difference between the polymer IE and dopant EA. That is, dopants with higher EAs result in higher doping efficiencies for the same polymer. To further investigate the influence of the dopant EA - polymer IE difference on the electrical conductivity, **Figure 4**a shows the electrical conductivity for all polymers investigated as a function of the dopant concentration. Given that PDPP-4T and PDPP-T-TT-T have more aromatic rings in their repeat units as compared to P3HT (6 rings vs. 1 ring), we present the dopant concentration as relative to the number of aromatic rings in the polymer backbone to allow for more direct comparisons between the polymers. Figure 4a shows that at low doping concentrations of 4 to 5%, $Mo(tfd)_3$ doping leads to electrical conductivities that are 15 to 800 times higher than for $FeCl_3$ doping with the same polymer. Furthermore, the difference between the electrical conductivity with $Mo(tfd)_3$ doping and $FeCl_3$ doping increases as the polymer IE increases. Figure 4b compares the ratio of σ with $Mo(tfd)_3$ doping at 1 to 5% to σ with $FeCl_3$ at 1 to 5% for the polymers as a function of polymer IE. The increasing $\sigma_{Mo(tfd)3}/\sigma_{FeCl3}$ ratio with polymer IE shows that the doping efficiency difference between $Mo(tfd)_3$ and $FeCl_3$ increases with IE, as expected based on simple energetic considerations.

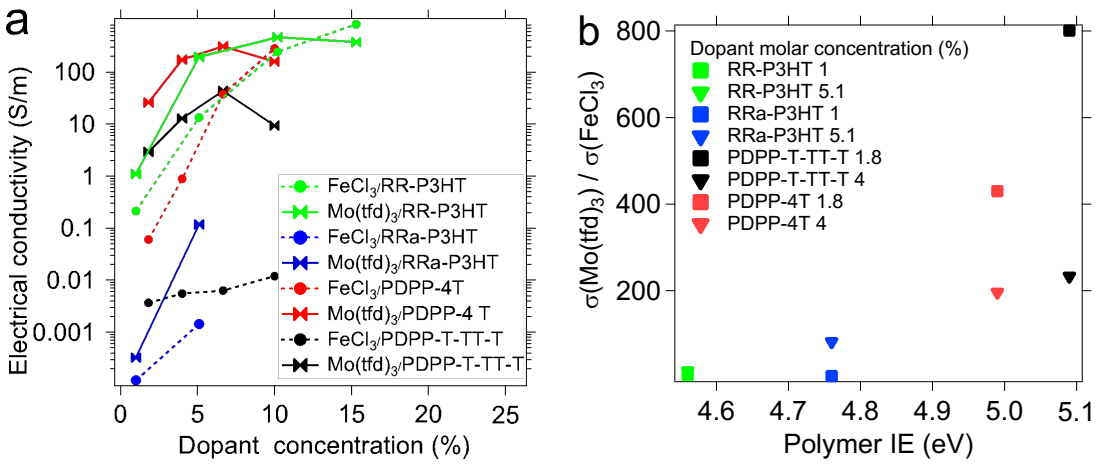

Figure 4. Electrical conductivity of $Mo(tfd)_3$ and $FeCl_3$ doped RR-P3HT, RRa-P3HT, PDPP-4T and PDPP-T-TT-T as a function of the dopant concentration (a) and the ratio of σ for $Mo(tfd)_3$ and $FeCl_3$ doped polymers at 1 to 5% dopant concentration as a function of the polymer IE (b).

2.3 Influence of the film morphology on the electrical conductivity

To a first order approximation the electrical conductivity corresponds with the number of polarons present. However, as discussed in section 2.2, it appears that the charge-carrier mobility also varies as a function of dopant. For example, the polaron band is twice as intense for $Mo(tfd)_3$ doped RR-P3HT as compared to $FeCl_3$ doped RR-P3HT, yet σ is 15 times greater. Part of the differences in charge-carrier mobilities may be from where the dopants are located and how the different dopants influence film crystallinity.[18,48] To investigate the morphology differences between the solution doped films with varying dopants, grazing incidence wide angle X-ray scattering (GIWAXS) was used to probe the crystalline order of the doped RR-P3HT films (**Table** 1 and SI **Figure S4, S5**). The π-π stacking distance (010) contracts upon dopant addition for all three dopants. At 5% this contraction varies from 0.06 to 0.09 Å for the three doped samples as compared to undoped RR-P3HT. As the dopant concentration increases further to 15%, the π-π stacking distances are largely unchanged from the 5% doped samples for the Mo complex dopants. By contrast, the 15% $FeCl_3$ doped RR-P3HT shows an additional 0.09 Å contraction in the π-π stacking distance from the 5% $FeCl_3$

doped film. This comparison between the 5% and 15% doped samples agrees with the UV-vis absorbance and electrical conductivity data to further support that $FeCl_3$ can continue to dope RR-P3HT at concentrations above 10%, whereas the ability of the Mo complexes to dope RR-P3HT saturates at between 5 and 10%. The origin of this decrease in the π-π stacking distance is polaron stabilization.[18] Essentially, the RR-P3HT backbones are pulled closer together, which allows the neighboring chains to more effectively stabilize the positively charged polarons.

Table 1. In and out-plane X-ray scattering peaks of doped RR-P3HT from GIXRD

Doped RR P3HT Molar fraction	d-spacing (Å) (010)	d-spacing (Å) (100)	d-spacing (Å) (200)	d-spacing (Å) (300)
RR-P3HT	3.81	16.01	8.02	5.36
$FeCl_3$ 5%	3.72	16.75	8.48	5.65
$FeCl_3$ 15%	3.62	17.69	8.86	5.97
$Mo(tfdCO_2Me)_3$ 5%	3.73	18.13	9.19	6.11
$Mo(tfdCO_2Me)_3$ 15%	3.75	17.69	9.35	6.12
$Mo(tfd)_3$ 5%	3.75	17.83	9.19	6.07
$Mo(tfd)_3$ 15%	3.75	17.69	9.35	6.12

The lamellar stacking (100) distances increase from 16.01 to between 16.75 and 18.13 Å as RR-P3HT is doped at 5%. The lamellar stacking distance continues to increase for $FeCl_3$ doping as the dopant concentration is further increased from 5 and 15%, but slightly decreases as the Mo dopants are increased from 5 to 15%. The increase in lamellar spacing is only on the order of 1.6 to 2.1 Å in all Mo complex doped RR-P3HT samples, which should not be large enough to accommodate the Mo complexes (~11-14 Å diameter, SI **Figure S6**). The inability of the Mo complexes to intercalate between the P3HT crystalline sidechains is supported by previous work investigating fullerene intercalation, where the similarly large

size of C_{60} prevented intercalation.[62] Here, we propose that the Mo complexes are located at the edges of the crystalline regions or in the amorphous regions, which was the position recently argued by Scholes, et al. for F4TCNQ doping of RR-P3HT.[18] If this is indeed the case, then the increased lamellar stacking distance may originate partly from repulsive Coulombic interactions between the polarons in the crystalline regions. It is more difficult to hypothesize where the $FeCl_3^-$ anions, or potentially $Fe_2Cl_6^-$ or $FeCl_4^-$ anions,[63, 64] are located, as these are smaller (~3-6 Å diameter, SI Figure S6) and may be able to intercalate between the P3HT sidechains within the crystalline regions.

In single-solution doped RR-P3HT, the doped polymers may aggregate with the anionic dopants,[17] with different dopants leading to different extents of solution aggregation and film morphologies. Atomic force microscopy images, displayed in SI **Figure S7**, of the single-solution doped RR-P3HT samples with 5% of the dopants show that the root mean squared (RMS) is nearly twice as high with $FeCl_3$ (10.4 nm) as with $Mo(tfd)_3$ (4.6 nm) and $Mo(tfd\text{-}CO_2Me)$ (6.3 nm). One means of minimizing the morphological differences between the films with the varying dopants is to use sequential doping. In this method RR-P3HT films are first spun-cast from chlorobenzene and the film is then doped by spin coating a solution of $FeCl_3$ or $Mo(tfdCO_2Me)_3$ in acetonitrile on top of the film. $Mo(tfd)_3$ was not used, as it is not soluble in acetonitrile. Acetonitrile is a poor solvent for RR-P3HT and causes the amorphous regions to swell and uptake the dopant molecules, whereas the crystalline regions stay largely intact.[17, 18, 48] These sequentially processed films display nearly identical morphologies as probed with AFM and display similar RMS roughness values of 0.4 to 0.5 nm, as shown in SI **Figure S8**. Based on the absorbance measurements shown in SI **Figure S9**, the $Mo(tfdCO_2Me)_3$ (σ=56.2±1.1 S/m) doped RR-P3HT sample has a doping ratio between the $FeCl_3$ doped RR-P3HT samples that were prepared with 0.03 (σ=8.1±1.2 S/m) and 0.05 (σ=34.4±1.4 S/m) mg/mL $FeCl_3$ concentrations. This data shows the same trend as with the single-solution doped films, where the Mo complexes exhibit higher conductivity

than $FeCl_3$ doped samples at similar doping levels. The agreement in trends between sequentially doped and single-solution doped films suggests that the observed differences in electrical conductivity between $FeCl_3$ and Mo complex doped films are not solely due to varying degrees of crystallinity or connectedness of the crystalline regions.

Absorption measurements in the near-IR to mid-IR regions can shed further light on understanding the transport properties of the doped films by providing a probe for the degree of polaron delocalization. As the degree of polaron delocalization increases the polaron band in the mid-IR region (P_1, peak ~0.4 eV) will shift to lower energies.[18, 48] For solution doped RR-P3HT at 5% doping concentration, the Mo dopants show similar P_1 bands with peaks at *ca.* 0.29 eV, while with $FeCl_3$ the P_1 band is shifted to higher energies with a peak at 0.38 eV, as shown in **Figure 5**. The lower energy P_1 bands for the Mo complexes suggest that polarons are more delocalized than with $FeCl_3$ as the dopant.[18, 46] The same trend is evident with the sequentially doped samples as shown in SI Figure S9, which suggests that the bathochromic shift of the low energy polaron peak is not due to changes in the degree of crystallinity. Thus, we attribute the bathochromic shift in the polaron peak to the presence of a more delocalized polaron because of decreased polaron-anion coulombic interactions. This decreased coulombic interaction is expected from the larger size of the Mo complexes relative to the $FeCl_3$ ions, which results in a greater average separation between the charge on the Mo complex anion and the P3HT polaron.

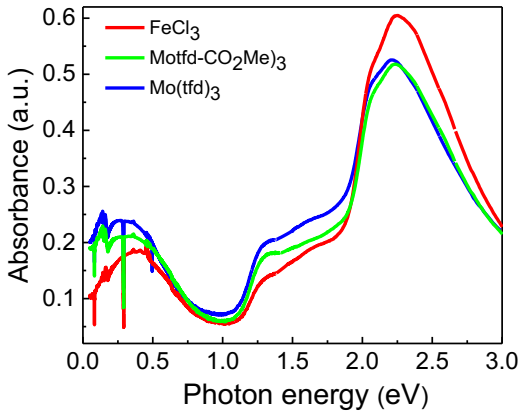

Figure 5. UV-Vis-IR absorbance spectra of single-solution doped RR-P3HT films.

An additional probe of polaron delocalization is the position of the Raman modes associated with the π-conjugated polymer backbone. As the polaron becomes more delocalized it weakens the bond strengths and results in lower energy stretching modes.[25, 65] The Raman spectra shown in **Figure 6** and SI **Figure S10** display distinctly different changes based on the dopant. For $Mo(tfd)_3$ and $Mo(tfd\text{-}CO_2Me)$ doped RR-P3HT the 1420-1450 cm^{-1} peak, which is attributed to $C_\alpha{=}C_\beta$ stretching vibrations, shifts from 1447 cm^{-1} in undoped RR-P3HT to 1425 and 1432 cm^{-1} for 10% doping with $Mo(tfd)_3$ and $Mo(tfd\text{-}CO_2Me)$, respectively. By contrast, the RR-P3HT sample doped with 10% $FeCl_3$ displays a more broadened Raman peak with a maximum that is shifted by only 1 cm^{-1} relative to undoped RR-P3HT. The significant broadening of the $FeCl_3$ doped RR-P3HT may indicate varying degrees of polaron delocalization and an overall increase in the disorder of the RR-P3HT film.[48] The relatively large bathochromic shift in the Mo complex doped RR-P3HT as compared to the minimal peak shift observed with $FeCl_3$ doping further supports that both Mo complexes lead to more delocalized polarons relative to $FeCl_3$. Additional support that delocalization leads to the observed bathochromic shifts in the Raman modes is obtained through an analysis of the Raman spectra of doped RRa-P3HT, as shown in SI Figure S10. Here, due to the lack of crystallinity and the increased torsion angles in the polymer backbone, the polaron should be more localized than in RR-P3HT. Comparing $Mo(tfd)_3$ doped RRa-

P3HT and RR-P3HT we indeed see that the maximum bathochromic shift in $Mo(tfd)_3$ doped RRa-P3HT (*ca.* 10 cm^{-1}) is less than in RR-P3HT (23 cm^{-1}).

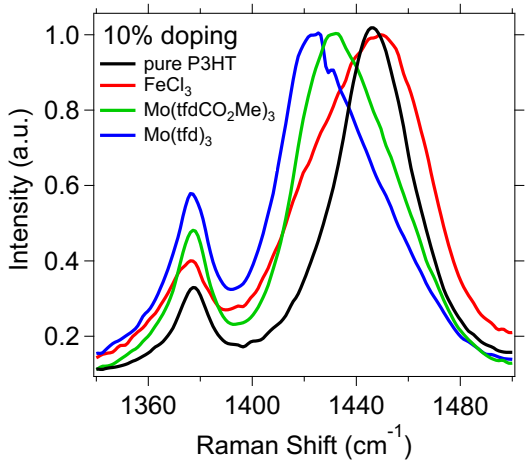

Figure 6. Raman spectra of RR-P3HT with 10% dopant concentrations. Excitation wavelength is 532 nm.

2.4 Influence of the dopant on the Seebeck coefficient and thermoelectric performance

The thermoelectric performance parameters for RR-P3HT with the different dopants are displayed in **Figure 7** as a function of dopant concentration. The Seebeck coefficient and electrical conductivity are inversely related, i.e., as the electrical conductivity increases the Seebeck coefficient decreases. This trend arises as the Seebeck coefficient is determined by the average entropy carried per charge carrier, and the entropy carried is dependent on the separation between the transport states and the Fermi energy.[66, 67] In general as more charge carriers are introduced, the Fermi energy shifts closer towards the transport states (i.e., the HOMO edge in a p-type material) and therefore each charge-carrier transports less entropy. Figure 7a shows the Seebeck coefficient of the doped RR-P3HT films as a function of doping concentration. With all dopants α decreases by *ca.* 60% as the dopant concentration increases from 1 to 5%. The Seebeck coefficients largely plateaus between 5 and 15% dopant for the Mo complexes, which is consistent with the saturation of the electrical conductivities. By contrast, with $FeCl_3$ doping the Seebeck coefficient continues to decrease as the dopant concentration increases.

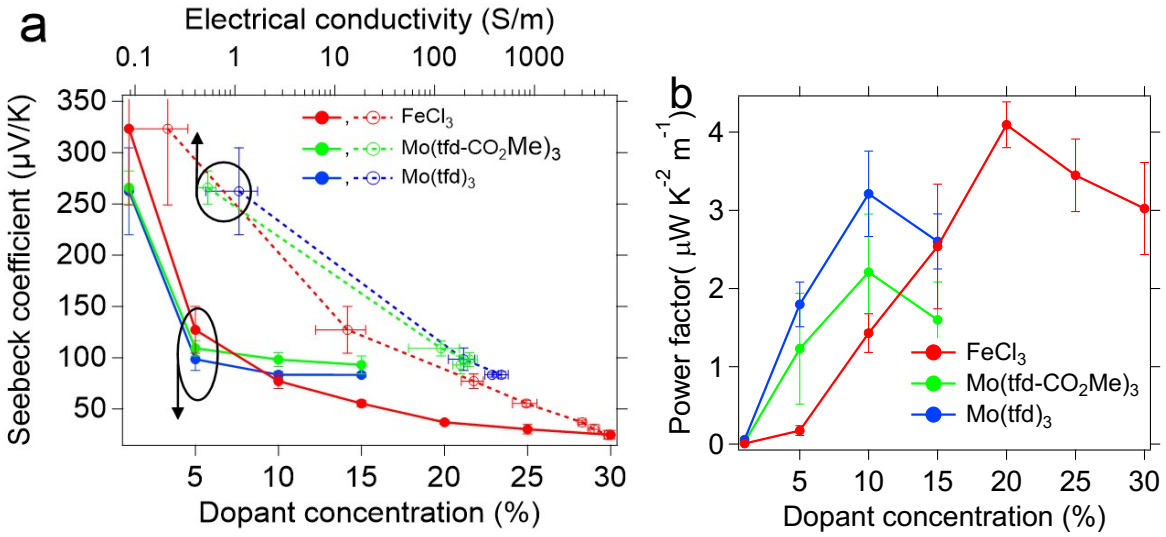

Figure 7: Seebeck coefficient vs. dopant concentration and electrical conductivity (a), and power factor vs. dopant concentration (b) for single-solution doped RR-P3HT with $FeCl_3$, $Mo(tfdCO_2Me)_3$, and $Mo(tfd)_3$.

The most important difference in terms of thermoelectric performance is that at 5% doping the Seebeck coefficients for all dopants are similar (all fall within 20% of the mean), despite the electrical conductivities being over an order of magnitude higher for the Mo containing dopants. As shown in Figure 7a, for the 5-15% dopant concentrations the RR-P3HT films doped with the Mo complexes display higher Seebeck coefficients than RR-P3HT doped with $FeCl_3$ at similar electrical conductivity. As a result, $Mo(tfd)_3$ doping results in a power factor that is *ca.*10 times higher than with $FeCl_3$ doping at 5% and 2.3 times higher at 10% doping. The higher power factors at low doping concentrations for the Mo complexes relative to $FeCl_3$ is most likely attributed to higher mobility charge-carriers in the Mo doped samples. Our reasoning is as follows: The position of the Fermi energy relative to the transport states will exert a large influence on the Seebeck coefficient, as particularly evident by models based on a transport edge where α increases directly with the energy separation between the Fermi energy and the transport edge. [67, 68] Neglecting changes to the density of states distributions imparted by the differing dopants, the position of the transport states

relative to the Fermi energy will be determined by the number of charge-carriers present. If the charge-carrier mobilities differ by an order of magnitude upon doping with two different dopants, then with the same number of polarons and similar Seebeck coefficients the material with the higher charge-carrier mobility will have an order of magnitude higher electrical conductivity. To further investigate this explanation, we turn to UPS measurements.

Ultraviolet photoelectron spectra of RR-P3HT, as displayed in **Figure 8** and **SI Figure S11**, probe the separation between the HOMO onset and the Fermi energy, as well as the work function and IEs. At low concentrations the work function and IE of doped RR-P3HT increase with dopant concentration, as shown in SI Figure S11g, S11h. As the dopant concentration is increased beyond 10%, the WF and IE of RR-P3HT doped with the Mo complexes do not change significantly, while the WF and IE of films doped with $FeCl_3$ continue increasing up to 30%. These trends in the WF and IE are consistent with the changes in electrical conductivity, and further support that $FeCl_3$ continues to further dope RR-P3HT at high doping concentrations. At 5% doping concentration Figure 8b shows that the positions of the HOMO onsets relative to the Fermi energies are similar with all dopants. With the difference between the transport states and Fermi energy playing a major role in determining the Seebeck coefficient, this UPS data supports that the Seebeck coefficients should be similar at this 5% doping concentration. At higher doping concentrations the HOMO onset continues to approach the Fermi energy, as shown in Figure 8a, particularly for $FeCl_3$ doping. In general, the continuously decreasing difference between the HOMO onset and Fermi energy for $FeCl_3$ doping agrees with the steady drop in the Seebeck coefficient with increasing $FeCl_3$ concentration.

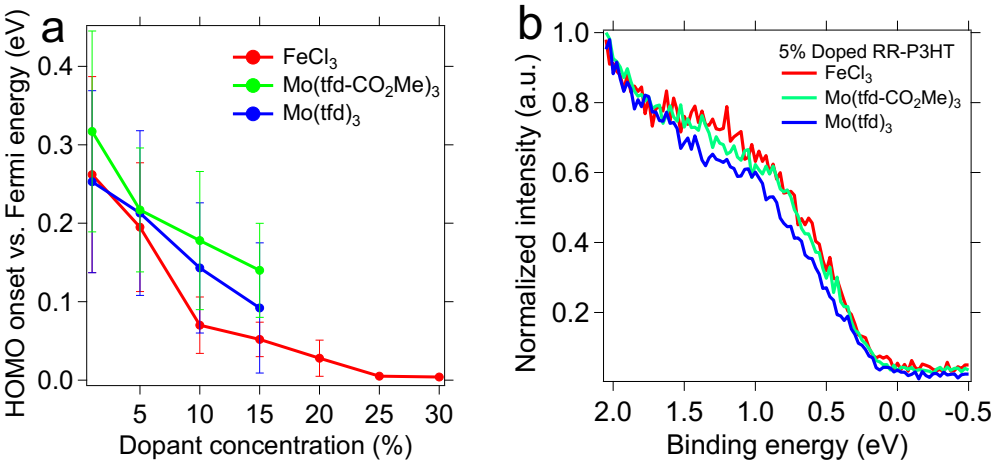

Figure 8: HOMO onset vs. Fermi energy (a) for RR-P3HT as a function of dopant concentration. Ultraviolet photoelectron spectra showing HOMO onset region (b) of 5% doped RR-P3HT.

In addition to RR-P3HT, we also looked at the influence of $Mo(tfd)_3$ and $FeCl_3$ on the thermoelectric performance of PDPP-4T, as shown in SI **Figure S12**. In PDPP-4T, $FeCl_3$ at low concentrations is not an effective dopant, as the electrical conductivity is two orders of magnitude lower than when $Mo(tfd)_3$ is used at the same dopant concentration. In support of the claim that σ is low for $FeCl_3$ doped PDPP-4T due to inefficient doping, we see that the Seebeck coefficient at 4% $FeCl_3$ doping is approximately four times greater than the Seebeck coefficient at 4% $Mo(tfd)_3$ doping. This contrasts with the results observed for the two dopants in RR-P3HT, where similar Seebeck coefficients were observed with both dopants at low concentrations. These trends in the Seebeck coefficients are in line with expectations of doping based on the dopant EA - polymer IE differences.

Like RR-P3HT, the power factor for $Mo(tfd)_3$ doped PDPP-4T also peaks at a relatively low dopant concentration of 6.7%, with the power factor reaching a respectable value of 15 μW K^{-2} m^{-1}, which is nearly five times greater than the maximum power factor obtained with $Mo(tfd)_3$ doped RR-P3HT. We attribute this peak in power factor at low dopant concentrations to the plateau in electrical conductivity. As with RR-P3HT, we suspect that this saturation in σ results from limited miscibility of $Mo(tfd)_3$ with PDPP-4T.

Surprisingly, PDPP-4T doped with $FeCl_3$ does reach high electrical conductivities of 1900 S/m at a $FeCl_3$ concentration of 20%, as compared to the maximum σ of 310 S/m obtained with $Mo(tfd)_3$ doping. Furthermore, the power factor of PDPP-4T with $FeCl_3$ doping surpasses that of PDPP-4T with $Mo(tfd)_3$ doping, reaching a value of 24 μW $K^{-2}m^{-1}$ at a doping concentration of 14.3% . These results show that despite the low EA of $FeCl_3$, it can still be an efficient dopant for higher IE polymers when used at high concentrations.

2.4 Mixed dopants for improved power factors

The power factors for RR-P3HT films doped with $Mo(tfd)_3$ appear limited by the saturation of the polaron density in RR-P3HT at only 5 to 10% dopant concentration. Thus, the power factor reaches a maximum at 10% doping with $Mo(tfd)_3$ as opposed to 20% with $FeCl_3$. Hypothetically, both $Mo(tfd)_3$ and $FeCl_3$ may be used simultaneously to dope P3HT and take advantage of the higher power factors achieved with $Mo(tfd)_3$ and the ability of $FeCl_3$ to more heavily dope RR-P3HT. Furthermore, $FeCl_3$ may intercalate into the crystalline regions, whereas $Mo(tfd)_3$ likely remains outside of the crystalline regions as discussed previously. Thus, these dopants present potentially complementary properties. To explore whether a mixed $FeCl_3$ and $Mo(tfd)_3$ dopant system may allow for higher thermoelectrical performance, we used 5% $Mo(tfd)_3$ with 5 to 25% $FeCl_3$. The electrical conductivities, Seebeck coefficients, and power factors of RR-P3HT with this mixed dopant system are shown in **Figure 9**.

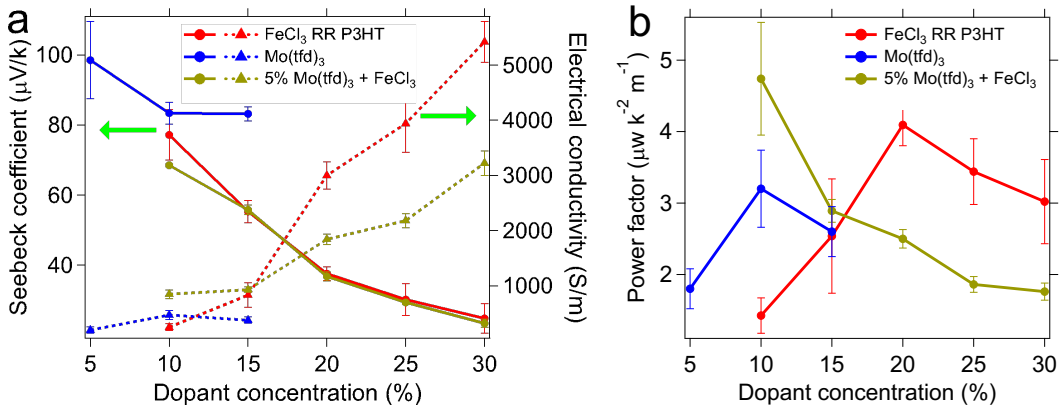

Figure 9: Electrical conductivity and Seebeck coefficient (a), and power factor (b) of RR-P3HT doped with $Mo(tfd)_3$, $FeCl_3$, and both 5% $Mo(tfd)_3$ and $FeCl_3$ combined.

At a total doping concentration of 10%, the mixed dopant film shows *ca.* 80% higher electrical conductivity than with only $Mo(tfd)_3$ and 250% higher than with only $FeCl_3$. Additionally, the Seebeck coefficient for this mixed dopant film is only 10% lower than with only $FeCl_3$. As a result, the mixed dopant film leads to the highest power factor for RR-P3HT observed in our hands. Additionally, relative to $FeCl_3$ as the only dopant, the use of mixed dopants reduces the amount of dopant necessary to reach the maximum power factor. As larger amounts of dopants can lead to poor film morphologies and decrease stability due to dopant diffusion, lower doping concentrations may be advantageous for the future development of organic thermoelectrics.

Conclusion

We find that the electrical conductivities of πCPs with low dopant concentrations are strongly influenced by the dopant EA – polymer IE difference; however, we find that at higher dopant loadings even low EA dopants can lead to high electrical conductivities. The fact that $FeCl_3$, with an EA of 4.6 eV can be used to dope PDPP-4T, which has an IE of 4.98 eV, and lead to electrical conductivities of nearly 2000 S/m is unexpected and shows that dopants with low EAs can still efficiently dope higher IE polymers. For all the πCPs investigated, we find that the electrical conductivity with $Mo(tfd)_3$ doping saturates at relatively low dopant concentrations of between 5 and 10%. At these low dopant

concentrations the electrical conductivity of the πCPs with $Mo(tfd)_3$ doping are up to 800 times greater than the electrical conductivity with $FeCl_3$ doping for the same polymer. We attribute the enhanced electrical conductivity with $Mo(tfd)_3$ to higher doping efficiency owing to the high EA, and also to increased polaron delocalization afforded by the larger dopant size and thus decreased coulomb interaction energy between the polaron and dopant anion. Overall, our results suggest that if the Mo complexes could effectively dope πCPs at higher dopant loadings, then superior electrical and thermoelectric properties should be achievable. In general, high EA dopants with large sizes that are highly miscible with conjugated polymers may provide a route to achieve high doping efficiencies at high dopant loadings. However, large dopants may also disrupt the crystallinity of πCPs at high loadings, thus further complicating the design of new dopants. As suggested in this paper, mixing small and large dopants may provide an approach that can be finely tuned to improve the thermoelectric performance of πCPs.

Supporting Information
Supporting Information is available from the Wiley Online Library or from the author.

Acknowledgments:
Acknowledgement is made to the donors of The American Chemical Society Petroleum Research Fund for partial support of this research. This material is based upon work supported in part by the National Science Foundation under Award No. DMR-1729737. J. M. appreciates the financial support from the National Science Foundation (Award number: 1653909) and startup funds from Purdue University

Received: ((will be filled in by the editorial staff))
Revised: ((will be filled in by the editorial staff))
Published online: ((will be filled in by the editorial staff))

Reference:

[1] S. R. Forrest, *Nature* **2004**, *428*, 911.
[2] B. Lüssem, M. Riede, K. Leo, *Phys. Status Solidi A* **2013**, *210*, 9.
[3] C. Wang, H. Dong, W. Hu, Y. Liu, D. Zhu, *Chem. Rev.* **2012**, *112*, 2208.
[4] J. Mei, Y. Diao, A. L. Appleton, L. Fang, Z. Bao, *J. Am. Chem. Soc.* **2013**, *135*, 6724.
[5] J. Rivnay, S. Inal, A. Salleo, R. M. Owens, M. Berggren, G. G. Malliaras, *Nat. Rev. Mater.* **2018**, *3*, 17086.
[6] S. Günes, H. Neugebauer, N. S. Sariciftci, *Chem. Rev.* **2007**, *107*, 1324.

[7] M. Li, K. Gao, X. Wan, Q. Zhang, B. Kan, R. Xia, F. Liu, X. Yang, H. Feng, W. Ni, Y. Wang, J. Peng, H. Zhang, Z. Liang, H.-L. Yip, X. Peng, Y. Cao, Y. Chen, *Nat. Photonics* **2016**, *11*, 85.
[8] B. Russ, A. Glaudell, J. J. Urban, M. L. Chabinyc, R. A. Segalman, *Nat. Rev. Mater.* **2016**, *1*, 16050.
[9] Q. Zhang, Y. Sun, W. Xu, D. Zhu, *Adv. Mater.* **2014**, *26*, 6829.
[10] A. M. Glaudell, J. E. Cochran, S. N. Patel, M. L. Chabinyc, *Adv. Energy Mater.* **2015**, *5*, 1401072.
[11] S. K. Gupta, P. Jha, A. Singh, M. M. Chehimi, D. K. Aswal, *J. Mater. Chem. C* **2015**, *3*, 8468.
[12] J. Mei, Z. Bao, *Chem. Mater.* **2014**, *26*, 604.
[13] G. Gustafsson, Y. Cao, G. M. Treacy, F. Klavetter, N. Colaneri, A. J. Heeger, *Nature* **1992**, *357*, 477.
[14] K. Walzer, B. Maennig, M. Pfeiffer, K. Leo, *Chem. Rev.* **2007**, *107*, 1233.
[15] O. Bubnova, Z. U. Khan, A. Malti, S. Braun, M. Fahlman, M. Berggren, X. Crispin, *Nat. Mater.* **2011**, *10*, 429.
[16] H. Shi, C. Liu, Q. Jiang, J. Xu, *Adv. Electron. Mater.* **2015**, *1*, 1500017.
[17] I. E. Jacobs, E. W. Aasen, J. L. Oliveira, T. N. Fonseca, J. D. Roehling, J. Li, G. Zhang, M. P. Augustine, M. Mascal, A. J. Moule, *J. Mater. Chem. C* **2016**, *4*, 3454.
[18] D. T. Scholes, P. Y. Yee, J. R. Lindemuth, H. Kang, J. Onorato, R. Ghosh, C. K. Luscombe, F. C. Spano, S. H. Tolbert, B. J. Schwartz, *Adv. Funct. Mater.* **2017**, *27*, 1702654.
[19] E. F. Aziz, A. Vollmer, S. Eisebitt, W. Eberhardt, P. Pingel, D. Neher, N. Koch, *Adv. Mater.* **2007**, *19*, 3257.
[20] J.-F. Chang, T. Sakanoue, Y. Olivier, T. Uemura, M.-B. Dufourg-Madec, S. G. Yeates, J. Cornil, J. Takeya, A. Troisi, H. Sirringhaus, *Phys. Rev. Lett.* **2011**, *107*, 066601.
[21] B. A. Bolto, R. McNeill, D. Weiss, *Aust. J. Chem.* **1963**, *16*, 1090.
[22] B. Bolto, D. Weiss, *Aust. J. Chem.* **1963**, *16*, 1076.
[23] H. Shirakawa, E. J. Louis, A. G. MacDiarmid, C. K. Chiang, A. J. Heeger, *J. Chem. Soc., Chem. Commun.* **1977**, 578.
[24] Z. Liang, M. J. Boland, K. Butrouna, D. R. Strachan, K. R. Graham, *J. Mater. Chem.A* **2017**, *5*, 15891.
[25] J. Yamamoto, Y. Furukawa, *J. Phys. Chem. B* **2015**, *119*, 4788.
[26] H. Koizumi, H. Dougauchi, T. Ichikawa, *J. Phys. Chem. B* **2005**, *109*, 15288.
[27] F. Huang, A. G. MacDiarmid, B. R. Hsieh, *Appl. Phys. Lett.* **1997**, *71*, 2415.
[28] Y. Qi, T. Sajoto, M. Kröger, A. M. Kandabarow, W. Park, S. Barlow, E.-G. Kim, L. Wielunski, L. C. Feldman, R. A. Bartynski, J.-L. Brédas, S. R. Marder, A. Kahn, *Chem. Mater.* **2010**, *22*, 524.
[29] K.-H. Yim, G. L. Whiting, C. E. Murphy, J. J. M. Halls, J. H. Burroughes, R. H. Friend, J.-S. Kim, *Adv. Mater.* **2008**, *20*, 3319.
[30] D. T. Duong, C. Wang, E. Antono, M. F. Toney, A. Salleo, *Org. Electron.* **2013**, *14*, 1330.
[31] P. Pingel, D. Neher, *Phys. Rev. B* **2013**, *87*, 115209.
[32] H. Méndez, G. Heimel, S. Winkler, J. Frisch, A. Opitz, K. Sauer, B. Wegner, M. Oehzelt, C. Röthel, S. Duhm, D. Többens, N. Koch, I. Salzmann, *Nat. Commun.* **2015**, *6*, 8560.
[33] R. Noriega, J. Rivnay, K. Vandewal, F. P. V. Koch, N. Stingelin, P. Smith, M. F. Toney, A. Salleo, *Nat. Mater.* **2013**, *12*, 1038.
[34] I. Salzmann, G. Heimel, M. Oehzelt, S. Winkler, N. Koch, *Acc. Chem. Res.* **2016**, *49*, 370.
[35] Y. Karpov, T. Erdmann, I. Raguzin, M. Al-Hussein, M. Binner, U. Lappan, M. Stamm, K. L. Gerasimov, T. Beryozkina, V. Bakulev, D. V. Anokhin, D. A. Ivanov, F. Günther, S. Gemming, G. Seifert, B. Voit, R. Di Pietro, A. Kiriy, *Adv. Mater.* **2016**, *28*, 6003.

[36] H. Méndez, G. Heimel, A. Opitz, K. Sauer, P. Barkowski, M. Oehzelt, J. Soeda, T. Okamoto, J. Takeya, J.-B. Arlin, J.-Y. Balandier, Y. Geerts, N. Koch, I. Salzmann, *Angew. Chem. Int. Ed.* **2013**, *52*, 7751.
[37] S. N. Patel, A. M. Glaudell, K. A. Peterson, E. M. Thomas, K. A. O'Hara, E. Lim, M. L. Chabinyc, *Sci. Adv.* **2017**, *3*.
[38] C.-Z. Li, C.-C. Chueh, F. Ding, H.-L. Yip, P.-W. Liang, X. Li, A. K. Y. Jen, *Adv. Mater.* **2013**, *25*, 4425.
[39] R. A. Schlitz, F. G. Brunetti, A. M. Glaudell, P. L. Miller, M. A. Brady, C. J. Takacs, C. J. Hawker, M. L. Chabinyc, *Adv. Mater.* **2014**, *26*, 2825.
[40] D. Kiefer, A. Giovannitti, H. Sun, T. Biskup, A. Hofmann, M. Koopmans, C. Cendra, S. Weber, L. J. Anton Koster, E. Olsson, J. Rivnay, S. Fabiano, I. McCulloch, C. Müller, *ACS Energy Lett.* **2018**, *3*, 278.
[41] L. Qiu, J. Liu, R. Alessandri, X. Qiu, M. Koopmans, R. A. Havenith, S. J. Marrink, R. C. Chiechi, L. J. Anton Koster, J. C. Hummelen, *J. Mater. Chem.A* **2017**, *5*, 21234.
[42] J. Hynynen, D. Kiefer, L. Yu, R. Kroon, R. Munir, A. Amassian, M. Kemerink, C. Müller, *Macromolecules* **2017**, *50*, 8140.
[43] J. Hynynen, D. Kiefer, C. Muller, *RSC Advances* **2018**, *8*, 1593.
[44] D. T. Duong, H. Phan, D. Hanifi, P. S. Jo, T. Q. Nguyen, A. Salleo, *Adv. Mater.* **2014**, *26*, 6069.
[45] R. Ghosh, C. M. Pochas, F. C. Spano, *J. Phys. Chem. C* **2016**, *120*, 11394.
[46] M. Wohlgenannt, X. M. Jiang, Z. V. Vardeny, *Phys. Rev. B* **2004**, *69*, 241204.
[47] S. Winkler, P. Amsalem, J. Frisch, M. Oehzelt, G. Heimel, N. Koch, *Mater. Horizons* **2015**, *2*, 427.
[48] A. R. Chew, R. Ghosh, Z. Shang, F. C. Spano, A. Salleo, *J. Phys. Chem. Lett.* **2017**, *8*, 4974.
[49] A. Salleo, R. J. Kline, D. M. DeLongchamp, M. L. Chabinyc, *Adv. Mater.* **2010**, *22*, 3812.
[50] Y. Zhao, X. Zhao, M. Roders, G. Qu, Y. Diao, A. L. Ayzner, J. Mei, *Chem. Mater.* **2015**, *27*, 7164.
[51] J. S. Ha, K. H. Kim, D. H. Choi, *J. Am. Chem. Soc.* **2011**, *133*, 10364.
[52] Y. Li, S. P. Singh, P. Sonar, *Adv. Mater.* **2010**, *22*, 4862.
[53] A. M. Boehm, J. Wieser, K. Butrouna, K. R. Graham, *Org. Electron.* **2017**, *41*, 9.
[54] H. Yoshida, *Chem. Phys. Lett.* **2012**, *539-540*, 180.
[55] X. Zhao, Y. Zhao, Q. Ge, K. Butrouna, Y. Diao, K. R. Graham, J. Mei, *Macromolecules* **2016**, *49*, 2601.
[56] Z.-L. Guan, J. B. Kim, H. Wang, C. Jaye, D. A. Fischer, Y.-L. Loo, A. Kahn, *Org. Electron.* **2010**, *11*, 1779.
[57] Y. Qi, T. Sajoto, S. Barlow, E.-G. Kim, J.-L. Brédas, S. R. Marder, A. Kahn, *J. Am. Chem. Soc.* **2009**, *131*, 12530.
[58] A. Dai, Y. Zhou, A. L. Shu, S. K. Mohapatra, H. Wang, C. Fuentes-Hernandez, Y. Zhang, S. Barlow, Y. L. Loo, S. R. Marder, B. Kippelen, A. Kahn, *Adv. Funct. Mater.* **2014**, *24*, 2197.
[59] C. M. Cardona, W. Li, A. E. Kaifer, D. Stockdale, G. C. Bazan, *Adv. Mater.* **2011**, *23*, 2367.
[60] A. Davison, N. Edelstein, R. H. Holm, A. H. Maki, *J. Am. Chem. Soc.* **1964**, *86*, 2799.
[61] M. L. Tietze, L. Burtone, M. Riede, B. Lüssem, K. Leo, *Phys. Rev. B* **2012**, *86*, 035320.
[62] K. R. Graham, C. Cabanetos, J. P. Jahnke, M. N. Idso, A. El Labban, G. O. Ngongang Ndjawa, T. Heumueller, K. Vandewal, A. Salleo, B. F. Chmelka, A. Amassian, P. M. Beaujuge, M. D. McGehee, *J. Am. Chem. Soc.* **2014**, *136*, 9608.
[63] A. Bhattacharya, A. De, S. N. Bhattacharya, S. Das, *J. Phys.: Condens. Matter* **1994**, *6*, 10499.

[64] A. Proń, Z. Kucharski, C. Budrowski, M. Zagórska, S. Krichene, J. Suwalski, G. Dehe, S. Lefrant, *J. Chem. Phys.* **1985**, *83*, 5923.
[65] G. Louarn, M. Trznadel, J. P. Buisson, J. Laska, A. Pron, M. Lapkowski, S. Lefrant, *J. Phys. Chem.* **1996**, *100*, 12532.
[66] M. Cutler, N. F. Mott, *Phys. Rev.* **1969**, *181*, 1336.
[67] H. Fritzsche, *Solid State Commun.* **1971**, *9*, 1813.
[68] S. D. Kang, G. J. Snyder, *Nat. Mater.* **2016**, *16*, 252.

The electrical conductivity and thermoelectric performance of doped conjugated polymers is shown to increase with dopant size and dopant electron affinity for doping concentrations of ≤10%; however, smaller dopants are able to more effectively dope the polymers at doping concentrations of ≥15%. Combining dopants of varying sizes is demonstrated as a route to increase the thermoelectric performance.

Keywords: conducting polymer, organic thermoelectric, doping, photoelectron spectroscopy, charge transport

Zhiming Liang, Yadong Zhang, Maryam Souri, Xuyi Luo, Alex M. Boehm, Ruipeng Li, Yan Zhang, Tairan Wang, Doo-Young Kim, Jianguo Mei, Seth R. Marder, Kenneth R. Graham

Influence of dopant size and electron affinity on the electrical conductivity and thermoelectric properties of a series of conjugated polymers

ToC figure

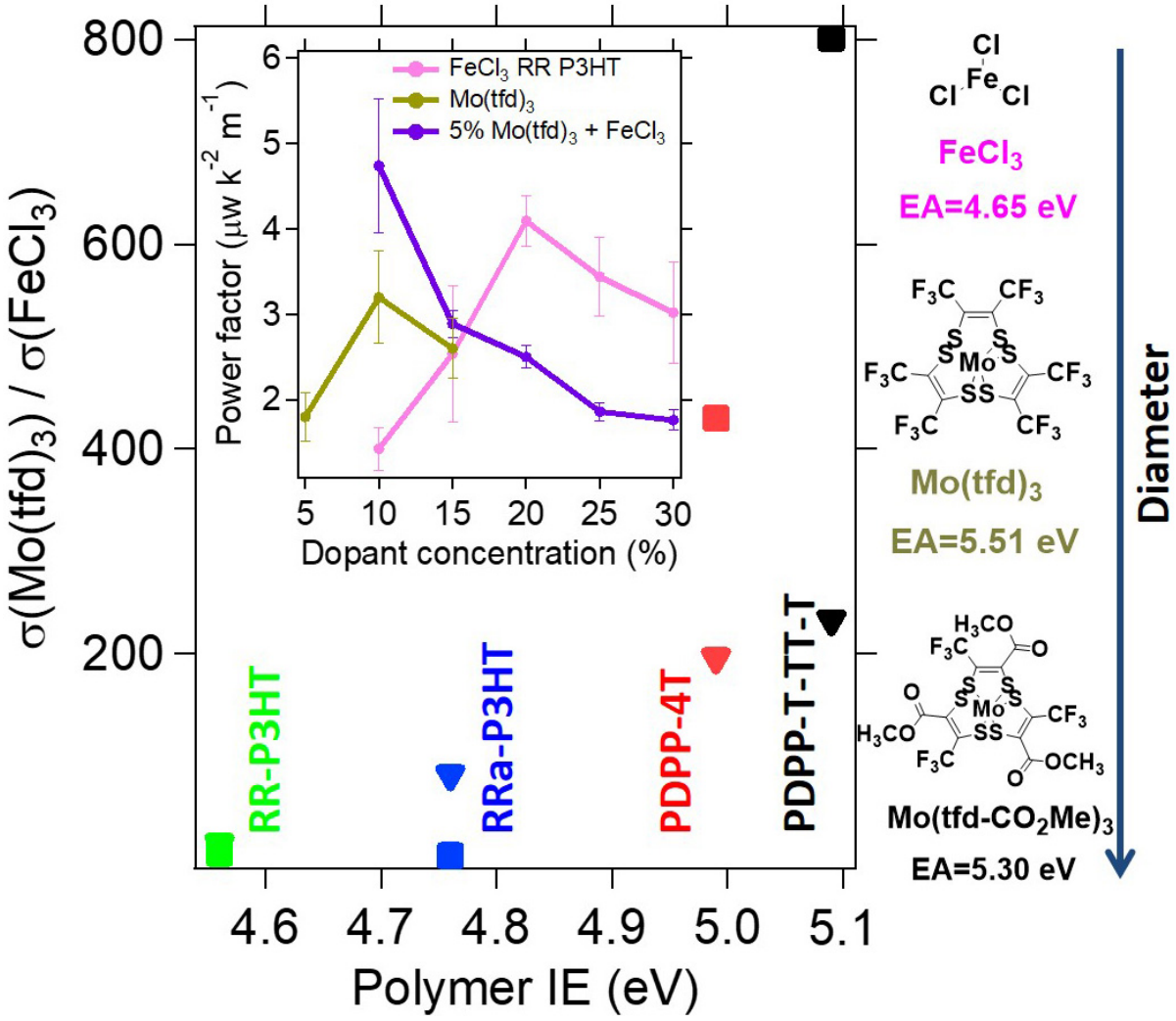

Supporting Information

Influence of dopant size and electron affinity on the electrical conductivity and thermoelectric properties of a series of conjugated polymers

*Zhiming Liang, Yadong Zhang, Maryam Souri, Xuyi Luo, Alex M. Boehm, Ruipeng Li, Yan Zhang, Tairan Wang, Doo-Young Kim, Jianguo Mei, Seth R. Marder, Kenneth R. Graham**

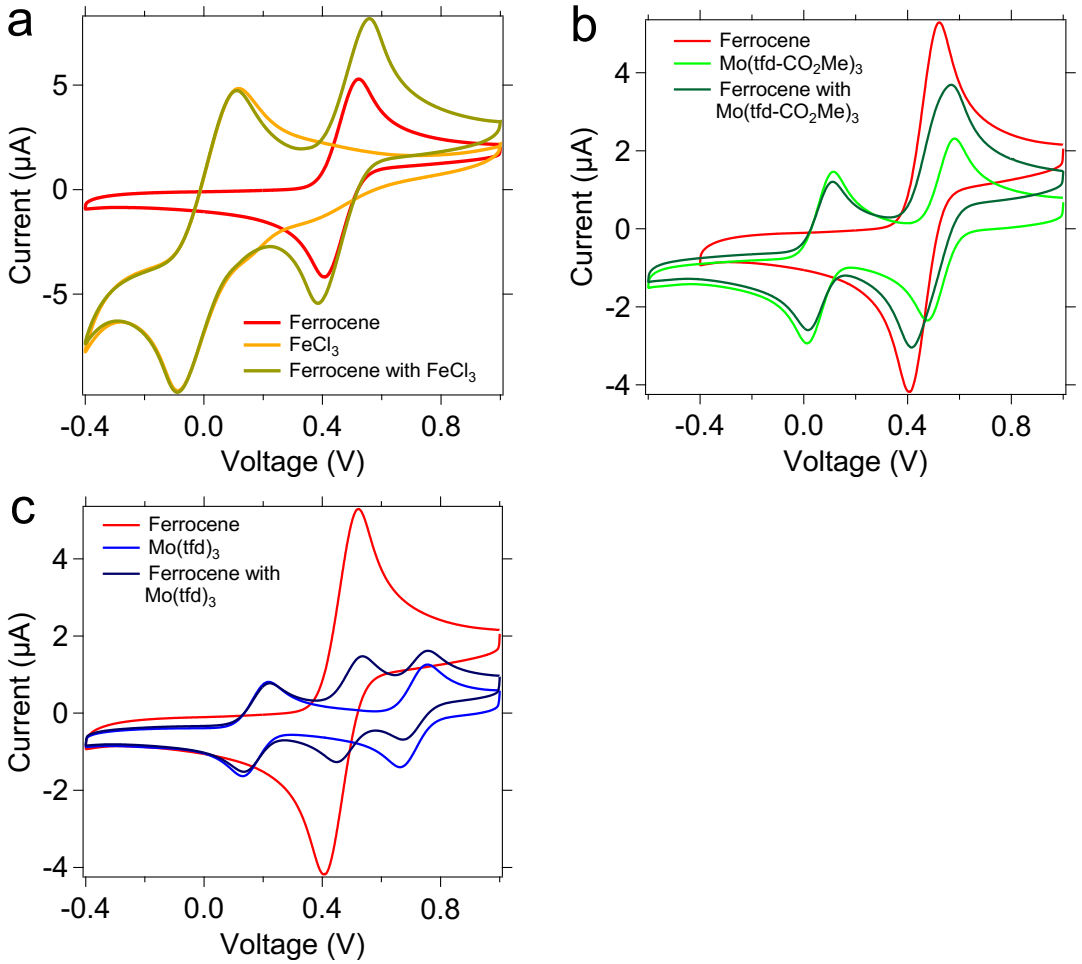

Figure S1: CV of polymers and dopants. a) $FeCl_3$ and ferrocene, b)$Mo(tfdCO_2Me)_3$ and ferrocene, c) $Mo(tfd)_3$ and ferrocene.

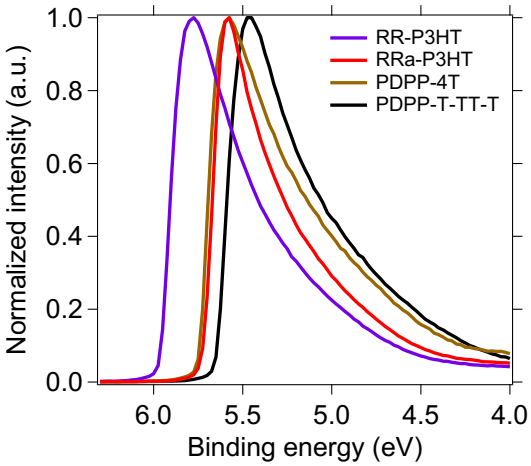

Figure S2: UPS spectra of the SECO region of the polymers.

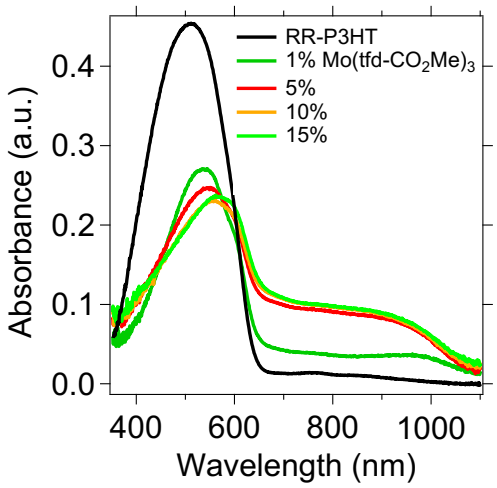

Figure S3: UV-Vis absorbance of Mo(tfdCO_2Me)$_3$ doped RR-P3HT.

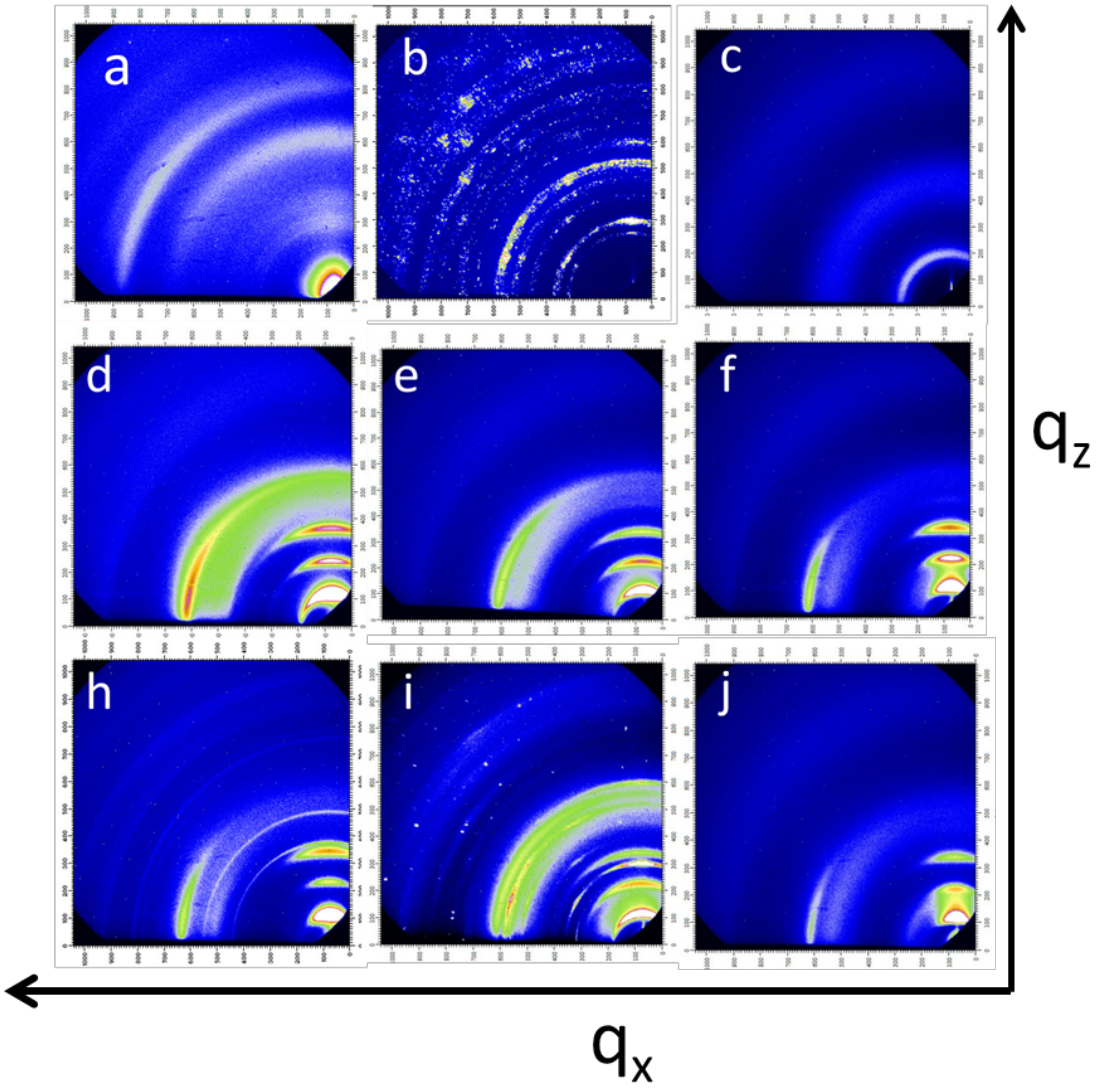

Figure S4: GIWAXS of dopants and doped RR P3HT. a) pure FeCl3, d) 5%, and h) 15% FeCl3 doped RR P3HT; b) pure $Mo(tfd)_3$, e) 5%, and i) 15% $Mo(tfd)_3$ doped RR P3HT; c) pure $Mo(tfd\text{-}CO_2Me)_3$, f) 5%, and j) 15% $Mo(tfd\text{-}CO_2Me)_3$ doped RR P3HT;

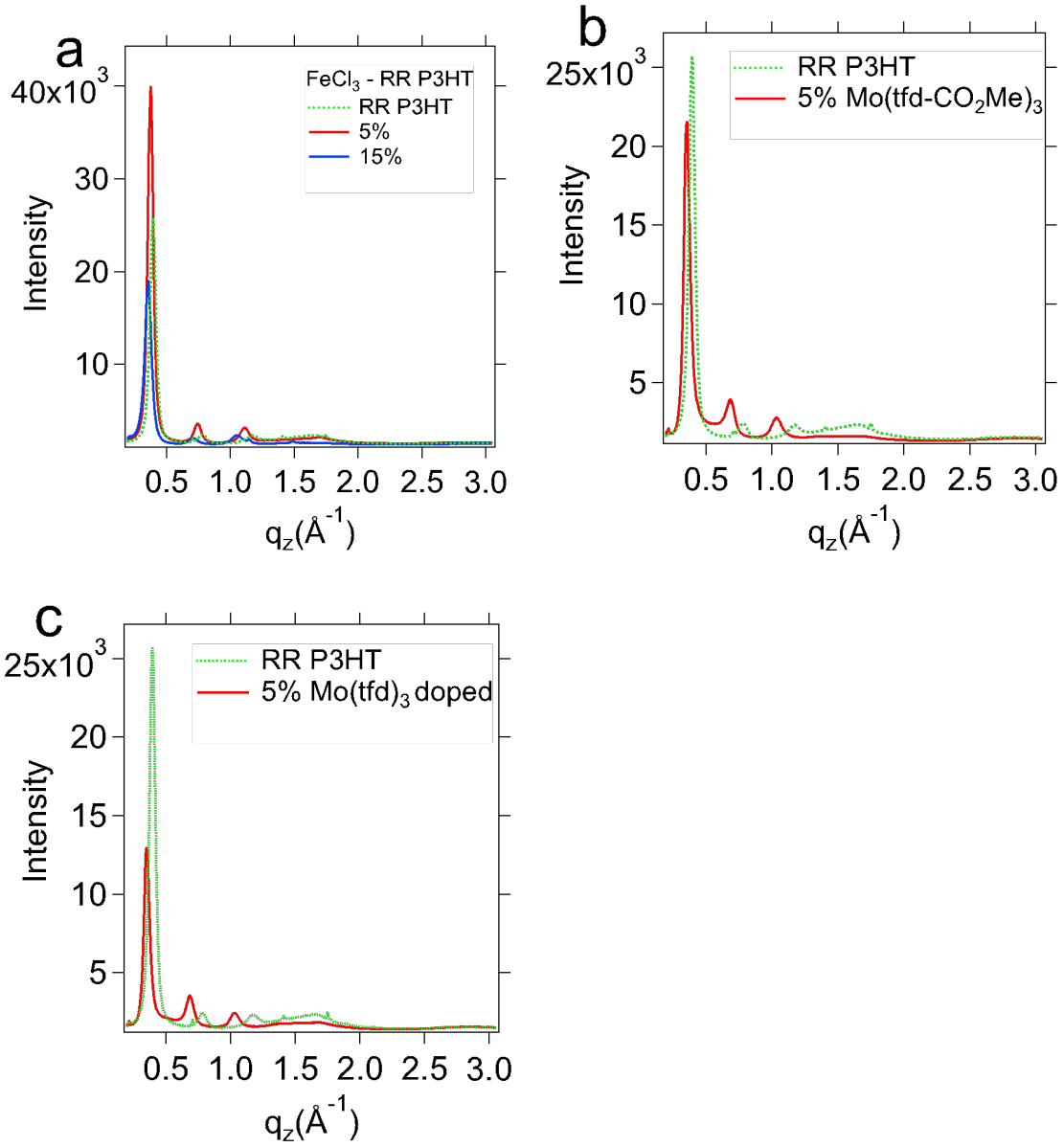

Figure S5: GIWAXS of doped RR-P3HT. (out of plane integrated intensity over 60 – 90 degree cake slice)

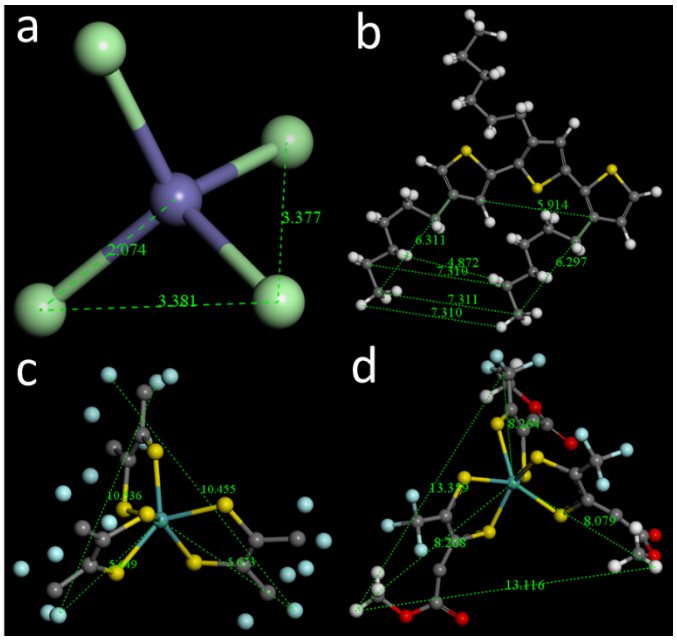

Figure S6: Chemical structure of dopants. a) $FeCl_4^-$, b) three repeating units of P3HT, c) $Mo(tfd)_3$,and d) $Mo(tfd\text{-}CO_2Me)_3$. These structures are geometry optimized by *ab initio* code Dmol3 in Materials studio. LDA (local density approximation) is chosen as the approximation to the exchange and correlation energy functional. SCF (Self-consistent field) tolerance is $1.0*10^{-6}$ Ha. These optimized values are comparable to some similar X-ray structure in the references)[1, 2]

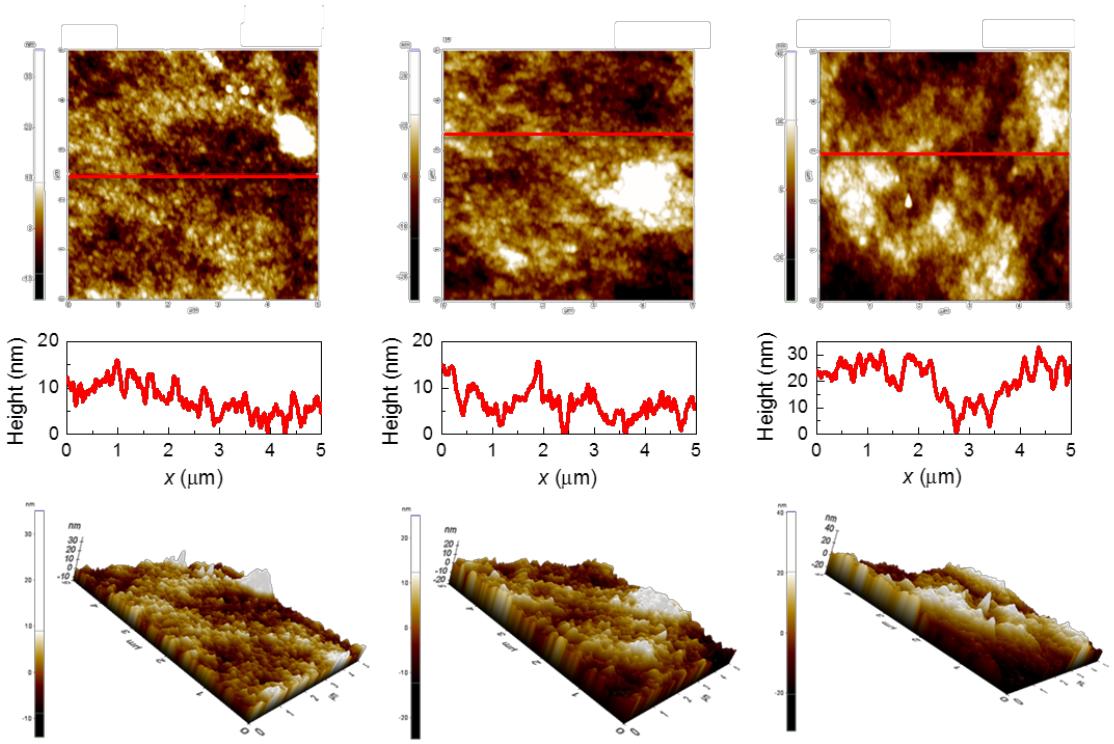

$Mo(tfd)_3$ Rq(nm) = 4.586 $Mo(tfdCO_2Me)_3$ Rq(nm) = 6.285 $FeCl_3$ Rq(nm) = 10.418

Figure S7: AFM images of 5% molar fraction $FeCl_3$, $Mo(tfd)_3$, and $Mo(tfdCO_2Me)_3$ doped RR P3HT.

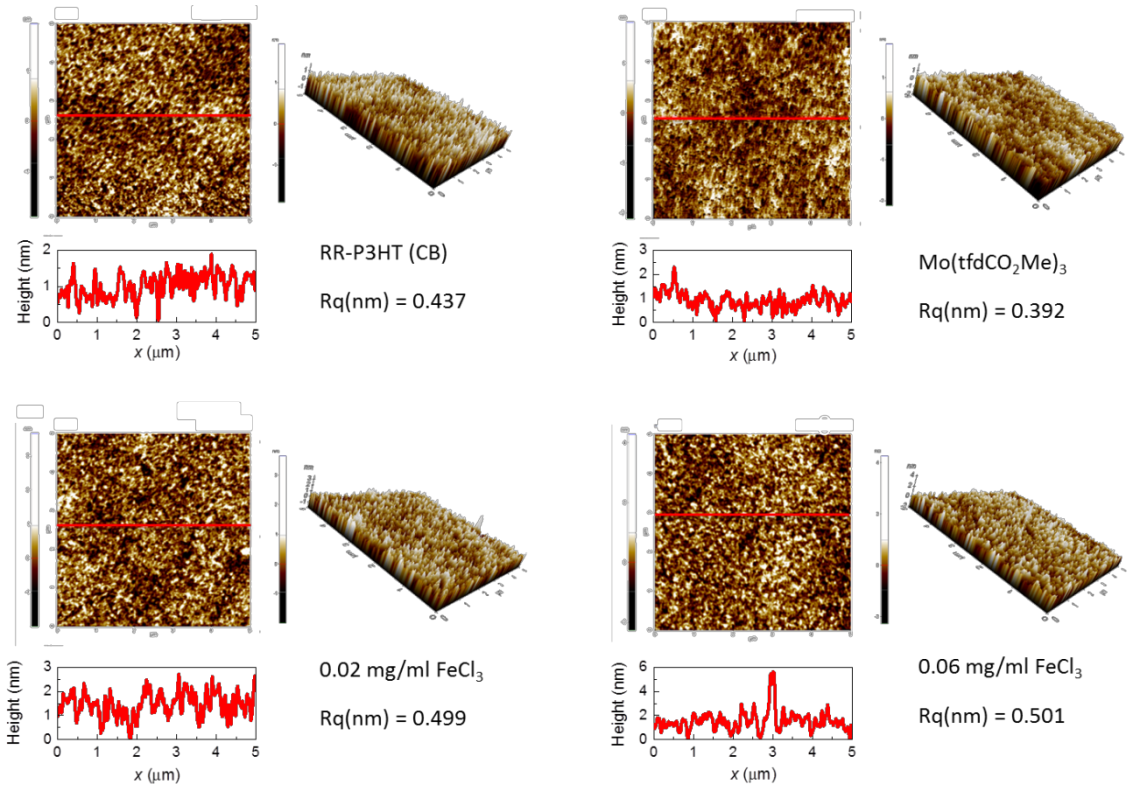

Figure S8: AFM images of sequential processing $FeCl_3$, and Mo(tfd-$CO_2Me)_3$ doped RR-P3HT.

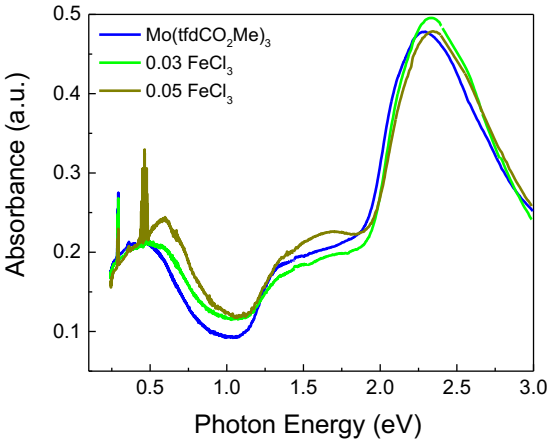

Figure S9. UV-Vis-IR absorbance spectra of sequentially doped RR-P3HT.

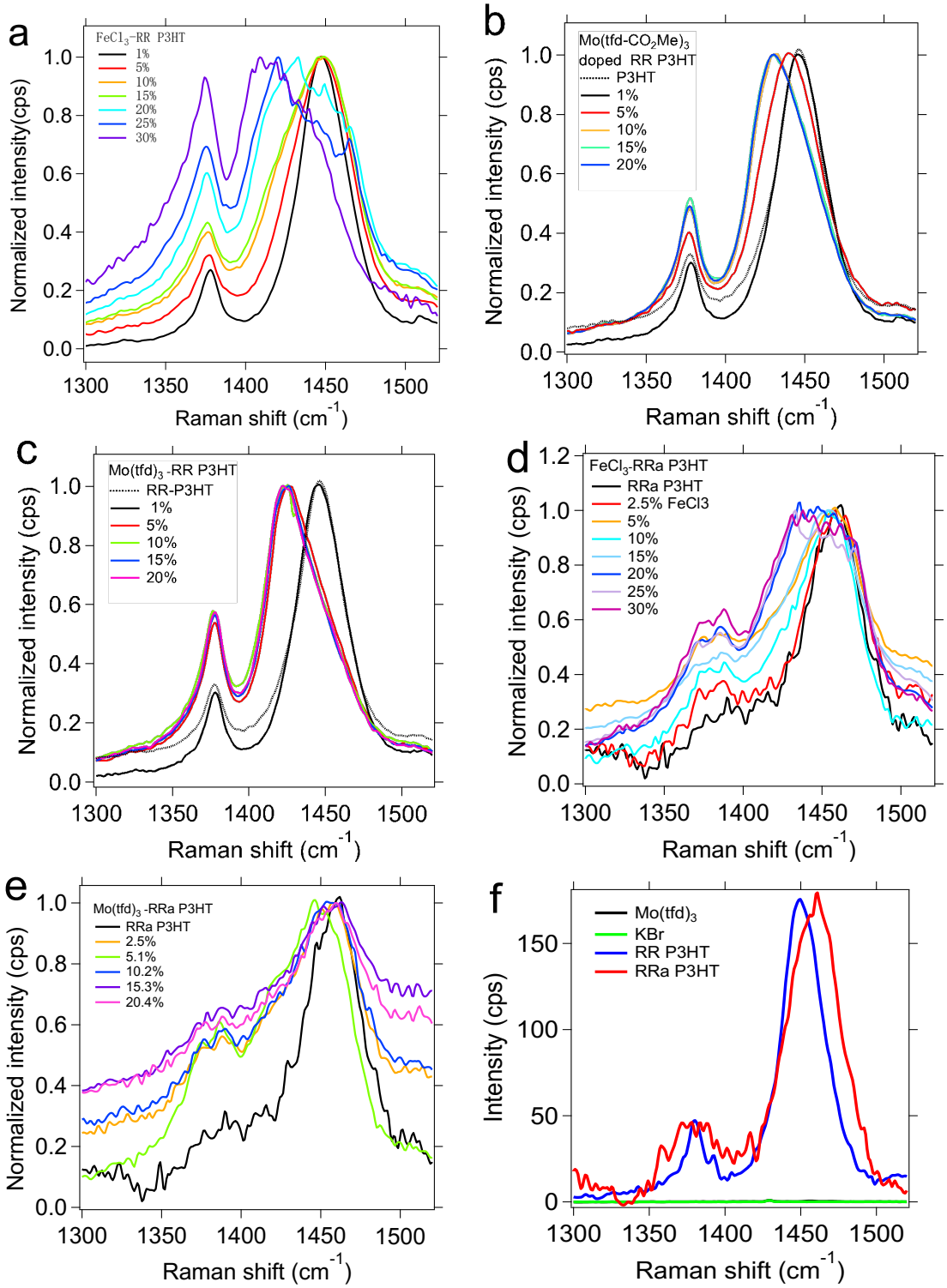

Figure S10. Raman spectra (532 nm Laser): a)$FeCl_3$-RR P3HT, b) $Mo(tfdCO_2Me)_3$-RR P3HT, c) $Mo(tfd)_3$-RR P3HT, d) $FeCl_3$-RRa P3HT, e) $Mo(tfd)_3$-RRa P3HT, f) RR, RRa P3HT, and $Mo(tfd)_3$.

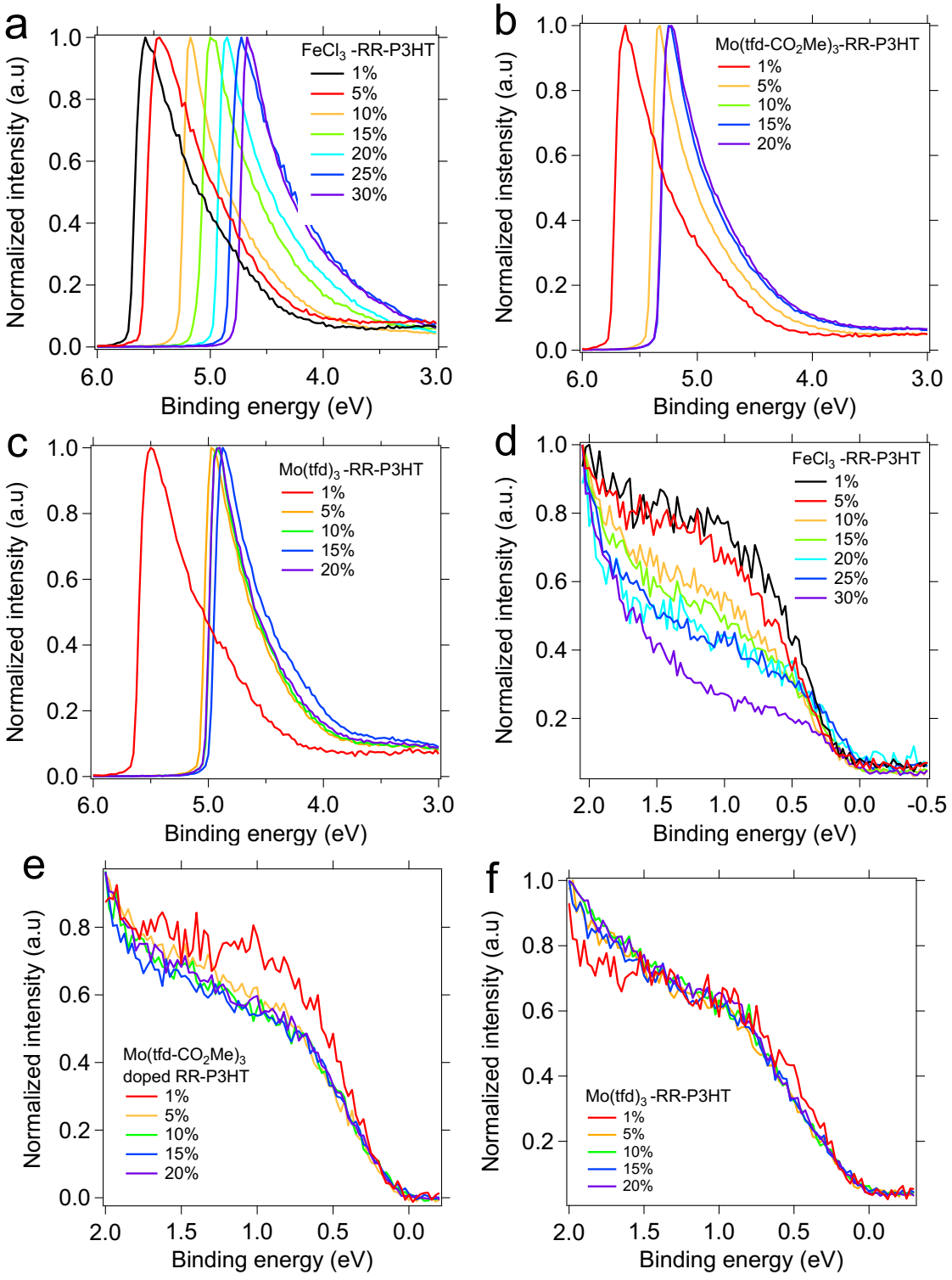
a
Normalized intensity (a.u)
Binding energy (eV)
FeCl3 -RR-P3HT
1%
5%
10%
15%
20%
25%
30%
b
Normalized instensity (a.u)
Binding energy (eV)
Mo(tfd-CO2Me)3-RR-P3HT
1%
5%
10%
15%
20%
c
Normalized intensity (a.u)
Binding energy (eV)
Mo(tfd)3 -RR-P3HT
1%
5%
10%
15%
20%
d
Normalized intensity (a.u.)
Binding energy (eV)
FeCl3 -RR-P3HT
1%
5%
10%
15%
20%
25%
30%
e
Normalized intensity (a.u)
Binding energy (eV)
Mo(tfd-CO2Me)3
doped RR-P3HT
1%
5%
10%
15%
20%
f
Normalized intensity (a.u)
Binding energy (eV)
Mo(tfd)3 -RR-P3HT
1%
5%
10%
15%
20%

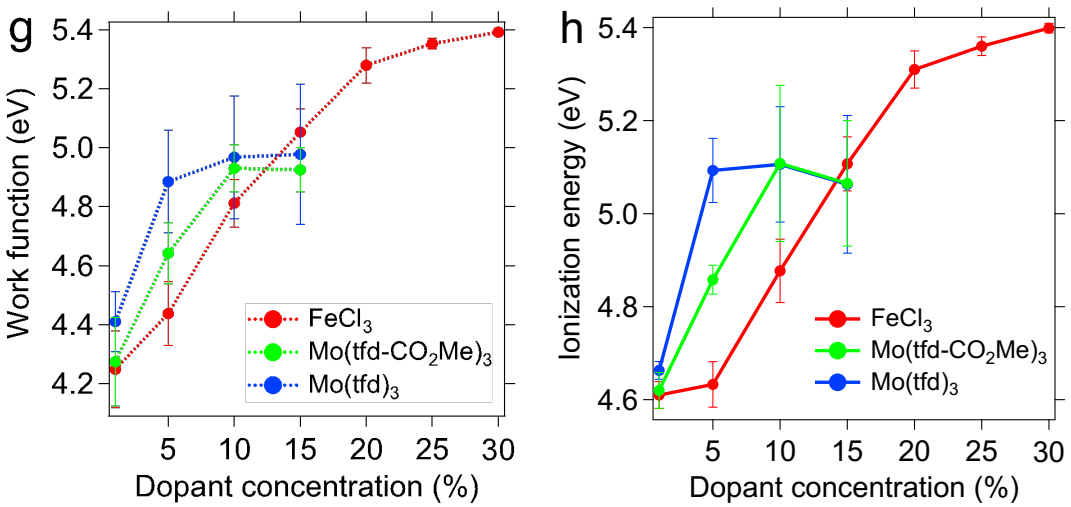

Figure S11: SECO and HOMO onset of $FeCl_3$(a,d), $Mo(tfdCO_2Me)_3$ (b,e), and $Mo(tfd)_3$ (c,f) doped RR-P3HT; Summarized Work function (g),and IE (h).

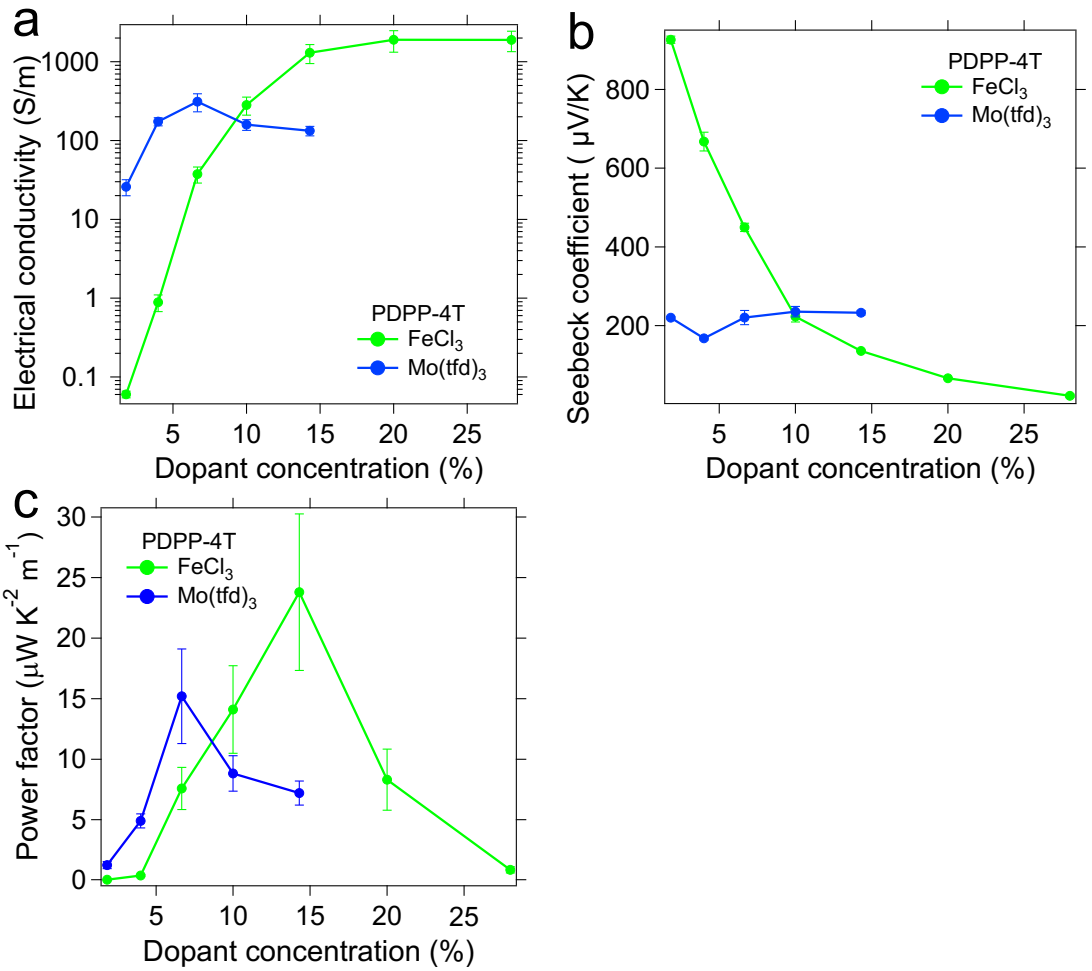

Figure S12. Electrical conductivity vs. dopant concentration (a), Seebeck coefficient vs. dopant concentration (b), and power factor vs. dopant concentration (c) for solution processing doped PDPP-4T with $Mo(tfd)_3$, and $FeCl_3$.

Experimental Section:

Materials. RR-P3HT and RRa-P3HT(Rieke metals); iron(III) chloride (anhydrous, 98%, crystalline, Alfa Aesar); chloroform (Anhydrous, DriSolv); acetonitrile (>99.5%, Sigma-aldrich); chlorobenzene (Anhydrous, DriSolv); bismuth(99.99%, Kurt J.Lesker). $Mo(tfd)_3$ and $Mo(tfdCO_2Me)_3$ was synthesized as previous publications.[3, 4] The synthesis of PDPP-4T and PDPP-T-TT-T also followed the previous references [5, 6]

Film preparation and doping.

Single-Solution processing:

P3HT was dissolved in chloroform with a concentration of 15 mg/ml; PDPP-4T, PDPP-T-TT-T, $FeCl_3$, and $Mo(tfdCO_2Me)_3$ were dissolved in chloroform with a concentration of 5 mg/ml; and $Mo(tfd)_3$ was dissolved in chloroform at 3 mg/ml. The doped solutions were stirred on a hotplate at 40 °C for 10 hours before the films were fabricated by drop-casting the solutions onto glass substrates. Films thicknesses ranged from 2 to 4 µm. All steps were completed in a nitrogen filled glovebox with H_2O < 0.1ppm, and O_2 < 0.1 ppm.

Sequential processing doping:

RR-P3HT was dissolved in chlorobenzene with a concentration of 15 mg/ml; $FeCl_3$, and $Mo(tfdCO_2Me)_3$ were dissolved in acetonitrile at 5 mg/ml. RR-P3HT was spin-cast at 3000 rpm for 30 seconds; then $FeCl_3$, or $Mo(tfdCO_2Me)_3$ solutions were dropped on top of the RR-P3HT films and let sit for 10 seconds before spinning off the dopant solution at 3000 rpm for 30 seconds. Films thicknesses ranged from 40 to 60 nm. All steps were carried out in a nitrogen filled glovebox with H_2O < 0.1ppm, and O_2 < 0.1 ppm.

Film characterization.

UPS measurements were conducted in a PHI 5600 UHV system with an 11 inch diameter hemispherical electron energy analyzer with multichannel detector. The photon source for the UPS measurements was an Excitech H Lyman-α lamp (E-LUX^{TM}121) coupled with a 90º

ellipsoidal mirror (E-LUX^{TM} EEM Optical Module) with a dry nitrogen purge of the beam path at 7.5 - 8.5 Torr, as detailed in a previous publication.[7] All UPS measurements were recorded with -5V sample bias and a pass energy of 5 eV. IPES measurements were performed using the Bremsstrahlung isochromat mode with electron kinetic energies below 5 eV to minimize sample damage. The low energy electron beam was generated using a Kimball Physics ELG-2 electron gun equipped with a low temperature (1150K) BaO cathode. Emitted photons were collected and focused with a fused silica bi-convex lens into the photon detector that consisted of an optical bandpass filter (214 nm, Andover corporation) and a photomultipler tube (R585, Hamamatsu Photonics). The IPES measurement was performed with a custom LabVIEW program. During all IPES measurements the UHV chamber was blacked-out to exclude external light and samples were held under a -20 V bias.

Grazing incidence wide angle X-ray scattering:

Grazing incidence wide-angle X-ray scattering measurements were carried out on the X9 beamline at the National Synchrotron Light Source, Brookhaven National Laboratory. Samples were perepared by drop casting doped polymer films following the

Electrical conductivity and Seebeck coefficient measurements:

Sheet resistance was measured with a four-point probe setup (Signatone S302-4, Keithley 2450 source meter); film thicknesses were measured with a Dektak D6M/32 profilometer.[8]

A custom-built setup was used to check Seebeck coefficient (more information in our previously report).[8] 100 nm bismuth (calibrated α = -62.1 μV/K) and 50 nm of gold which work as the electrodes and electrical contact pads was thermally evaporated.

Optical absorbance:

UV-Vis absorbance spectra were measured with an Ocean Optics QE Pro high performance spectrometer; Raman spectra were measured with a thermo scientific DXR Smart-Raman.

UV-Vis-NIR absorbance spectra were measured at normal incidence using a grating-type spectrophotometer in the photon energy regions of 0.5–3eV at room temperature. The absorption spectra are calculated using $\alpha(\omega) = -Ln(\frac{T(\omega)_{film+sub}}{T(\omega)_{sub}})$.

Atomic Force Microscopy (AFM):

The samples were characterized using Park XE-70 Atomic Force Microscope.

CV measurements:

Cyclic voltammetric measurements were conducted in a single-compartment electrochemical cell with three electrodes: working electrode (glassy carbon, geometric area of 0.07 cm^2), reference electrode (Ag/AgCl) and the counter electrode (Pt wire). Cyclic voltammetric (CV) curves were recorded by an electrochemical workstation (CHI-760D, CH Instruments, Austin, TX). For working electrode, an active material was cast on glassy carbon current collector. The electrochemical measurements were recorded after purging with N_2 for 10 min. 0.1 M tetrabutylammonium hexafluorophosphate in chloroform was used as the supporting electrolyte. All sample had a concentration of *ca.* 0.2 mM and were measured with a scan speed of 50 $mV*s^{-1}$.

References:

[1] S. K. Mohapatra, Y. Zhang, B. Sandhu, M. S. Fonari, T. V. Timofeeva, S. R. Marder, S. Barlow, *Polyhedron* **2016**, *116*, 88.
[2] K. R. Dunbar, A. Quillevéré, *Angew. Chem. Int. Ed.* **1993**, *32*, 293.
[3] A. Davison, R. Holm, R. Benson, W. Mahler, *Inorganic Syntheses, Volume 10* **2007**, 8.
[4] A. Dai, Y. Zhou, A. L. Shu, S. K. Mohapatra, H. Wang, C. Fuentes‐Hernandez, Y. Zhang, S. Barlow, Y. L. Loo, S. R. Marder, *Adv. Funct. Mater.* **2014**, *24*, 2197.
[5] Y. Zhao, X. Zhao, Y. Zang, C.-a. Di, Y. Diao, J. Mei, *Macromolecules* **2015**, *48*, 2048.
[6] B. C. Schroeder, T. Kurosawa, T. Fu, Y. C. Chiu, J. Mun, G. J. N. Wang, X. Gu, L. Shaw, J. W. Kneller, T. Kreouzis, *Adv. Funct. Mater.* **2017**, *27*.
[7] A. M. Boehm, J. Wieser, K. Butrouna, K. R. Graham, *Org. Electron.* **2017**, *41*, 9.
[8] Z. Liang, M. J. Boland, K. Butrouna, D. R. Strachan, K. R. Graham, *J. Mater. Chem.A* **2017**, *5*, 15891.